INTERNATIONAL ACADEMIC RESEARCH AND STUDIES IN

CHEMISTRY

EDITOR **PROF. DR. EDIP BAYRAM**



Genel Yayın Yönetmeni / Editor in Chief · C. Cansın Selin Temana

Kapak & İç Tasarım / Cover & Interior Design · Serüven Yayınevi

Birinci Basım / First Edition • © Ekim 2025

ISBN • 978-625-5749-15-4

© copyright

Bu kitabın yayın hakkı Serüven Yayınevi'ne aittir.

Kaynak gösterilmeden alıntı yapılamaz, izin almadan hiçbir yolla çoğaltılamaz. The right to publish this book belongs to Serüven Publishing. Citation can not be shown without the source, reproduced in any way without permission.

Serüven Yayınevi / Serüven Publishing

Türkiye Adres / Turkey Address: Kızılay Mah. Fevzi Çakmak I. Sokak

Ümit Apt No: 22/A Çankaya/ANKARA

Telefon / Phone: 05437675765 web: www.seruvenyayinevi.com e-mail: seruvenyayinevi@gmail.com

Baskı & Cilt / Printing & Volume Sertifika / Certificate No: 47083

INTERNATIONAL ACADEMIC RESEARCH AND STUDIES IN

CHEMISTRY

OCTOBER 2025

EDITOR PROF. DR. EDIP BAYRAM

CONTENTS

MODELLING OF SOLID PHASE EXTRACTION PROCESSES OF ZINC (ZN) USING AMBERLITE XAD-4 RESIN WITH					
MULTIVARIATE POLYNOMIAL REGRESSION TI					
Berrin TOPUZ	•				
Sinan TOPÇAKAR	7				
INVESTIGATION OF THE ANTIBACTERIAL ACCONTEZOLID MOLECULE USING IN SILICO ME					
MOLECULAR DOCKING STUDI	ES				
Emel EKİNCİ					
Özlem GÜNDOĞDU AYTAÇ					
Sertan AYTAÇ	25				
INVESTIGATION OF THE EFFECTS OF MAGNES ON THE BORON NITRIDE FORMATION AT TH METHODS					
Muhammed ÖZ	45				



MODELLING OF SOLID PHASE EXTRACTION PROCESSES OF ZINC (ZN) USING AMBERLITE XAD-4 RESIN WITH MULTIVARIATE POLYNOMIAL REGRESSION TECHNIQUE (MPR).





Berrin TOPUZ¹ Sinan TOPÇAKAR²

¹ Doç. Dr.

² Doktora Öğrencisi

1. INTRODUCTION

Zinc (Zn) is a naturally occurring catalyst and an essential element in metabolic processes, including genetic activities and hormone production. Moreover, Zn(II) has been demonstrated to play a pivotal role in the metabolic processes of sugars, proteins, and cholesterol. (Rezaee and Tajer-Mohammad-Ghazvini,2022; Al-Murshedi et. al.,2025; Walther, et.al., 1998).

It is estimated that an adult weighing 70 kg retains approximately 2-3 g of Zn. It is widely accepted within the scientific community that Zn is considered a low-toxicity element for humans. The American Institute of Food and Nutrition has determined the maximum tolerable upper level of Zn intake for adults as 40 mg day-1. Zn is absorbed more effectively from liquids (up to approximately 70%) than from solid foods (approximately 30%), primarily in the small intestine. (Molenda and Kolmas, 2023). As the concentrations of zinc in food samples are typically below the detection limit of modern instrumental devices, it is essential to implement a preconcentration step prior to analysis. This process involves the elimination of matrix effects and the preparation of samples within the measurement range of the device being utilised. (Umaz et.al., 2025).

Many preconcentration approaches have been studied so far, including cloud point extraction, liquid phase microextraction, solid phase extraction (SPE), solid phase microextraction (SPME), coprecipitation, adsorption methods and chromatographic methods (Haq et. al., 2021). Among these, SPE has several advantages, including availability, short extraction times, low operating costs, high enrichment factors, low sample volumes, environmental friendliness and the elimination of toxic solvents (Buszewski and Szultka, 2012; Ozdemir et. al., 2018).

In the SPE method, the use of carbon nanotubes (Stafiej and Pyrzynska, 2008), magnetically charged polymeric materials (Mashhadizadeh and Karami, 2011), silica gel (Shemirani et. al., 2004), and Amberlite XAD resins (Saxena and Meena 2014; Ozdemir et. al., 2022; Zawierucha et. al., 2014) has been investigated for the determination of Zn(II).

Amberlite XAD adsorbents are characterised by their high degree of cross-linking, Macroreticulated polystyrene, aliphatic or otherwise. The polymer is synthesised from a phenol-formaldehyde condensate. Spherical polymers that exhibit elevated levels of porosity. XAD resins are distinguished by their high surface area, uniform pore size distribution,

and the presence of a copolymer backbone. The substance has been demonstrated to exhibit exceptional durability and resistance to acids, bases and oxidising agents. The material exhibits superior properties, including chemical stability (Ahmad et. al., 2015).

The field of data science is concerned with the analysis of data by applying scientific and mathematical principles to extract meaningful insights from experimental data. The findings obtained from this process are utilised for a variety of purposes, including the prediction of future behaviour based on past data, the identification of historical errors through scientific reasoning, the achievement of specific goals, and the understanding of the nature and magnitude of past events reflected in the data (Sarker, 2021). The utilisation of the Python programming language within the domain of data science is experiencing a marked increase in prevalence. The rationale behind the surge in Python's popularity can be attributed to its userfriendliness, extensive support network, and accessibility, even for individuals lacking a background in computer science (Cai et. al., 2005). Optimisation problems are a common issue across various scientific disciplines, including engineering, energy, chemistry, and physics. A range of algorithms are utilised to optimise a smooth function numerically, with the most suitable choice depending on factors such as computational speed, memory usage, and ease of implementation. Multivariate Polynomial Regression Modelling (MPR) is a sensitive surface analysis technique for prediction and correlation analysis, also known as data mining (Su and Peng, 2021).

The present study has employed the Multivariate Polynomial Regression (MPR) methodology in python environment in order to determine the optimal SPE conditions that will maximise the sorption and elution capacity of the stationary phase. This method utilised experimental data on the SPE method parameters that had been developed for the enrichment and separation of Zn(II) ions with Amberlite XAD-4 (AXAD-4) resin. At the same time, the mathematical relationship between the independent and dependent variables was expressed with clarity. The dithiozone (DTZ) reagent was employed for the UV-VIS spectrophotometric detection of preconcentrated and separated Zn(II) ion.

2. Experimental

2.1. Instrument, reagents and standards

In this study, the determination of zinc (II) contents was conducted utilising a UV-VIS spectrophotometer (Spektroquant Pharo 300 Merck) equipped with a 1 cm quartz cuvette by the dithiozone method for the determination of Zn(II) (Paradkar and Williams, 1994).

The pH measurements were conducted using an ISOLAB digital pH meter. The weighing process was conducted using a RADWAG brand scale, which exhibited a sensitivity of 0.00001. In the context of preconcentration studies, the BLUPUMP brand AKM pump was utilised for the purpose of adjusting the flow rate of a glass column measuring 10 cm in length and possessing an internal diameter of 1 cm.

AXAD-4 resin (with a surface area of 780 m²/g and a pore diameter of 5 nm) was purchased from Sigma-Aldrich (Milwaukee, WI, USA). Before use, AXAD-4 was cleaned with 10 ml methanol, 1 molL-1 HNO₃ (in acetone), 1 molL-1 NaOH, acetone, and deionized water, respectively, to remove both organic and inorganic residual contaminants. Then, it was washed and kept in an oven at 1050C until it dried. The dried Amberlit XAD-4 polymer is then in polyethylene bottles for use in studies has been preserved.

Zinc solutions used during the study were administered daily from stock standard solutions (Merck, 1000 mg/L, in 0.5 molL⁻¹ HNO₃) was prepared by diluting it. In order to examine the effect of pH on sorption on Amberlite XAD-4 resin, acetate buffer, 0.5 mol L⁻¹ HNO₃ and 0.5 mol L⁻¹ NH₃ solutions were used to adjust the pH of the loading solutions. A buffer solution was prepared by adding the appropriate amount of a 1 M solution of CH₃COOH to a 1 M solution of CH₃COONa, with the aim of adjusting the pH in the range of 4-6.

The absorbance of preconcentrated Zn(II) ions was measured using UV-VIS spectrophotometry with dithizone (DTZ) reagent (Merck, Darmstadt, Germany) at a wavelength of 520 nm and in the pH range of 4–6.

2.2. Preparation of column with AXAD-4 Resin

The inner diameter of the column is 1 cm, and the volume is 5 mL. The internal surface is coated with glass cotton and 0.2 g of AXAD-4. The resin is subsequently filled, with the upper portion of the resin being coated with glass cotton. The column was subjected to a cleaning and conditioning procedure involving nitric acid (1 mol L⁻¹), deionised water, hydrochloric acid (1 mol L-1), deionised water, and acetate buffer (pH 5) solutions. This procedure was conducted following metal adsorption experiment.

2.3.Method

The samples containing Zn(II) in volumes ranging from 50 to 1000 millilitres, adjusted to pH 4-6 with a setat buffer, were subjected to the prewashed and conditioned AXAD-4 column at varying flow rates. The Zn(II) ion present on the resin was eluted with varying flow rates and volumes of eluent solutions. UV-VIS spectrophotometric analyses were then performed by the ditizon method.

In this study, the MPR method was implemented in the Python environment to ensure optimal modelling of the elution and adsorption processes of the zinc element (Sinha, 2013). This methodology enabled the determination of the effects of multiple independent variables (e.g. pH, sample volume and flow rate, eluent flow rate, concentration and volume) on dependent variables (i.e. sorption and recovery efficiency).

3. Results and discussion

The results of the 15-step experimental study of the sorption and elution steps of the SPE method were plotted by obtaining equations referred to as the hypothesis function.

$$h_{\theta}(x_1, x_2, x_3) = \theta_0 + \theta_1 x_1 + \theta_2 x_1^2 + \theta_3 x_2 + \theta_4 x_2^2 + \theta_5 x_3 + \theta_6 x_3^2 + \theta_7 x_1 x_2 + \theta_8 x_1 x_3 + \theta_9 x_2 x_3$$
(1)

The equation was utilised to formulate a general system hypothesis function from the data obtained. The terminology is explained as follows:

- $h_{\theta}(x_1, x_2, x_3)$ represents the percentage of recovery obtained in both the adsorption and elution stages.
- x_1 denotes the pH level during the adsorption phase, while it indicates the flow rate in the elution phase.
- x_2 corresponds to the flow rate in the adsorption stage, whereas it represents the sample volume in the elution stage.
- x_3 signifies the sample volume during the adsorption process, while it denotes the concentration in the elution process.
- $\theta_0 \theta_9$ coefficients symbolize the statistical parameters in the regression analysis.

For a clearer representation, the hypothesis function can also be expressed as follows:

$$h_{\theta}(x) = \theta_0 + \theta_1 x_1 + \theta_2 x_2 + \theta_3 x_3 + \theta_4 x_4 + \theta_5 x_5 + \theta_6 x_6 + \theta_7 x_7 + \theta_8 x_8 + \theta_9 x_9$$
(2)

The main goal is to minimize the least squares difference between actual values and predicted values (Hastie and Tibshirani, 2009; Montgomery et. al., 2021). For this, we have a cost function as follows (equation 3):

$$J(\theta) = \frac{1}{2} \sum_{i=1}^{15} \left(h_{\theta}(x^{(i)}) - y^{(i)} \right)^2 \tag{3}$$

In this context, the i values represent the numerical measurement values obtained from the relevant experiments. As there are 15 measurements, they are written from 1 to 15 inclusive. In this particular experiment, y represents the numerical recovery value.

After creating the model, parameters θ values must be found. For this purpose, the normal equation solution was used. The optimal solution is given below (4):

$$\theta = (X^T X)^{-1} X^T y \tag{4}$$

Here matrix X is represented as:

$$\begin{split} X \\ &= \begin{bmatrix} 1 & x_1{}^{(1)} & x_1{}^{(1)2} & x_2{}^{(1)} & x_2{}^{(1)2} & x_3{}^{(1)} & x_3{}^{(1)2} & x_1{}^{(1)}x_2{}^{(1)} & x_1{}^{(1)}x_3{}^{(1)} & x_2{}^{(1)}x_3{}^{(1)} \\ \vdots & \vdots & \vdots & \vdots & \vdots & \vdots & \vdots & \vdots & \vdots \\ 1 & x_1{}^{(15)} & x_1{}^{(15)2} & x_2{}^{(15)2} & x_2{}^{(15)2} & x_3{}^{(15)} & x_3{}^{(15)2} & x_1{}^{(15)}x_2{}^{(15)} & x_1{}^{(15)}x_2{}^{(15)} & x_1{}^{(15)}x_3{}^{(15)} & x_2{}^{(15)}x_3{}^{(15)} \\ \end{split}$$

The vector **y** is as follows:

$$\mathbf{y} = \begin{bmatrix} y^{(1)} \\ y^{(2)} \\ \vdots \\ y^{(15)} \end{bmatrix}$$

Finally, the θ vector, which contains the coefficients we aim to estimate, is expressed as:

$$m{ heta}_{1} = egin{bmatrix} heta_{0} \ heta_{1} \ heta_{2} \ heta_{3} \ heta_{4} \ heta_{5} \ heta_{6} \ heta_{7} \ heta_{8} \ heta_{9} \ \end{pmatrix}$$

After the parameter values were determined, the developed model achieved R^2 values of 0.81 for sorption and 0.86 for elution. These values were considered acceptable, taking into account both the potential risk of overfitting arising from the limited number of experiments and the explanatory capacity of the model.

Once the required θ parameters for building the hypothesis function $h_{\theta}(x)$ were obtained, the next step was to identify the key input variables x_1, x_2 and x_3 that maximize the function's output. To locate this global optimum, the differential evolution algorithm (Storn and Price,1995) was employed. All mathematical operations were implemented in the Python environment.

Through this procedure, the highest value of the hypothesis function was determined along with the corresponding input variables x_1 , x_2 and x_3 that generate this peak. Keeping these inputs fixed, six three-dimensional plots were produced: three representing the sorption process (Figures 1–3) and three for the elution process (Figures 4–6).

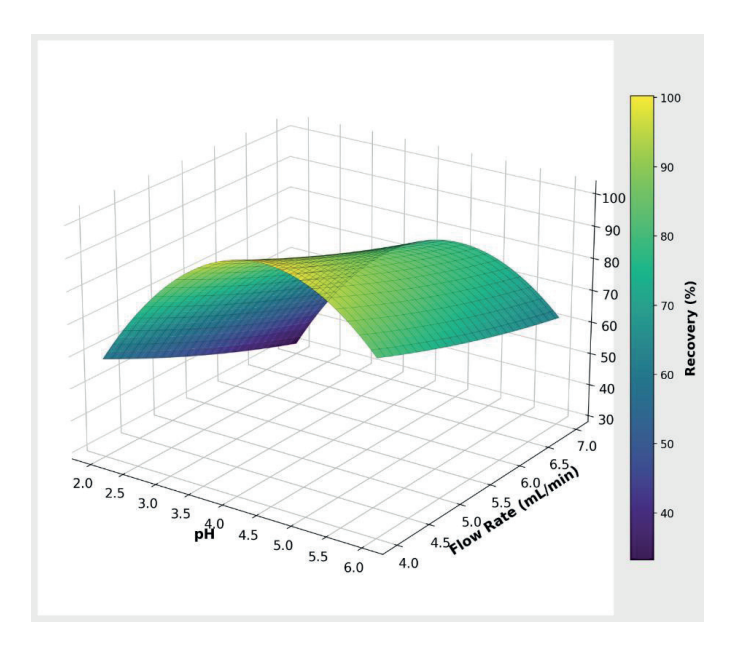


Fig. 1. Effect of sample pH and flow rate on Zn(II) recovery in the sorption process.

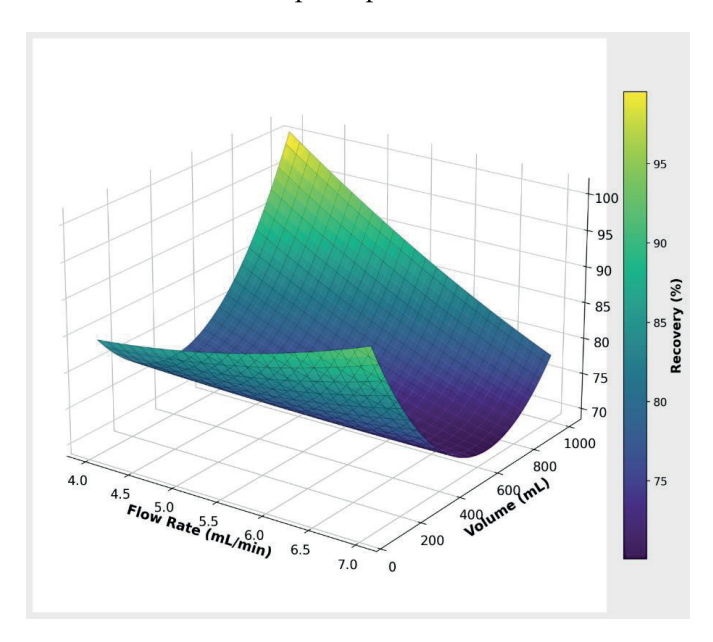


Fig. 2. Effect of sample flow rate and volume on Zn(II) recovery in the sorption process.

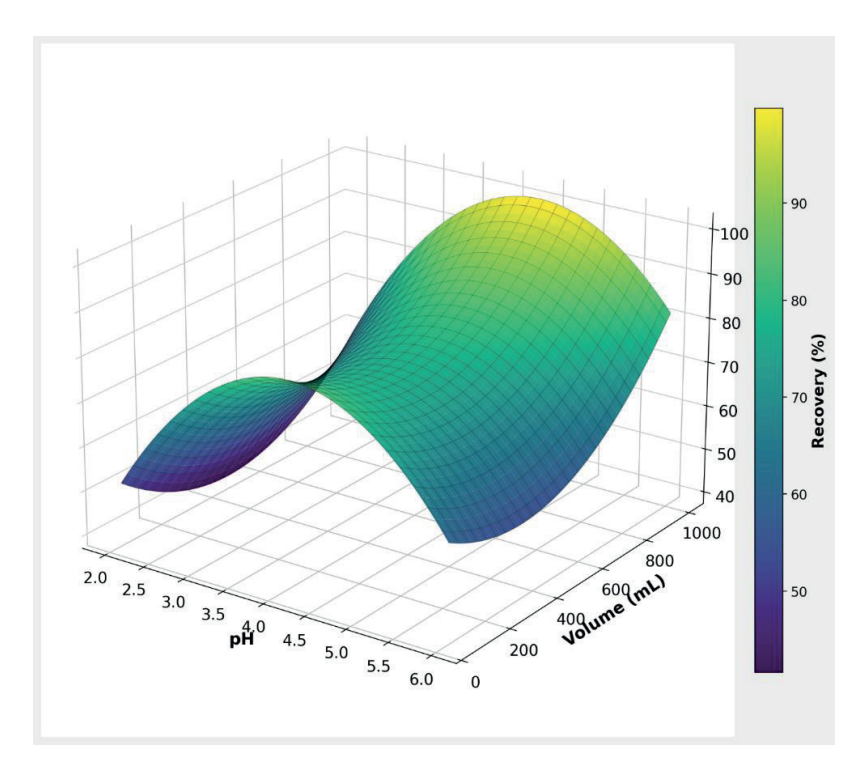


Fig. 3. Effect of sample pH and volume on Zn(II) recovery in the sorption process.

The present study investigates the effect of three independent variables (pH, volume and flow rate) on the adsorption of Zn(II) ions with the recovery values on AXAD-4 resin.

In Figure 1, where the sample volume is kept constant (volume=1000 ml) and the effects of pH and flow rate are examined, it is observed that changes in pH have a much higher impact on the recovery value. Additionally, a significant recovery decrease occurring in regions where pH is below and above 4.4 is another important detail.

When the effects of flow rate and volume are examined while the pH value is kept constant at pH=4.39 (Figure-2), it is observed that both variables have different effects in different regions of the graph. Therefore, it would

be incorrect to say that one variable is definitely more effective than the other.

The final analysis of the sorption process relates to Figure 3, where the flow rate is kept constant and the effects of pH and volume are examined. A distinct saddle shape is observed here. In regions where recovery is high, both variables have a similar effect. However, in regions where recovery is low, the most significant factor is the distance from the pH value of 4.39. In this case, it can be said that pH has a more significant overall effect.

Therefore, the pH value is the variable with the highest effect in the general context of the sorption process.

As demonstrated in the figures, the optimum values for achieving maximum recovery were obtained at a pH of 4.39, a flow rate of 4 ml/min, and a sample volume of 1000 ml. When these optimum variables were selected, the maximum recovery was found to be 100.57%.

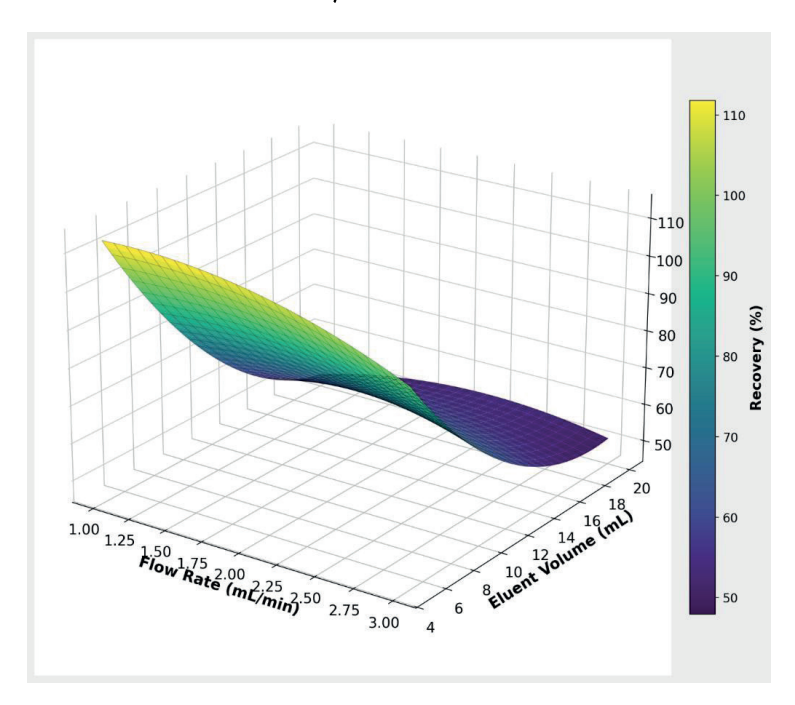


Fig. 4. Effect of eluent flow rate and volume on Zn(II) recovery in the elution process.

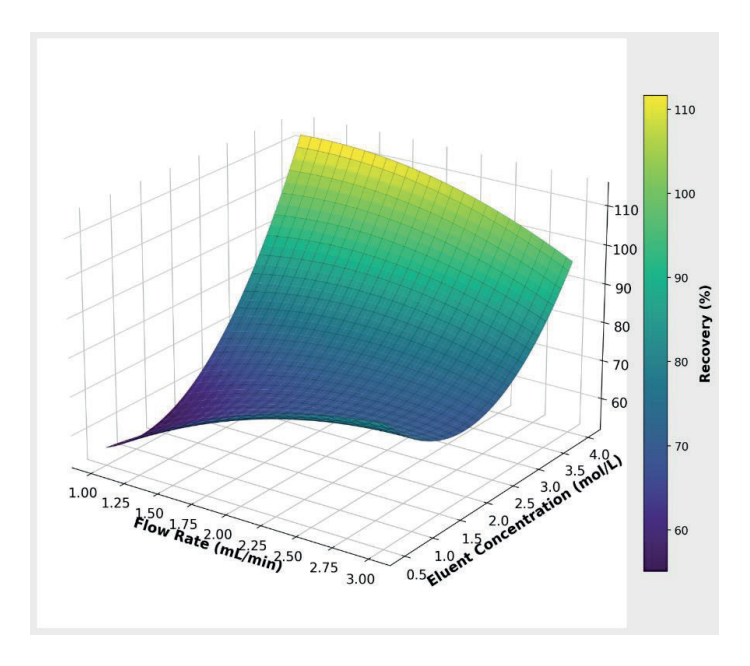


Fig. 5. Effect of eluent flow rate and concentration on Zn(II) recovery in the elution process.

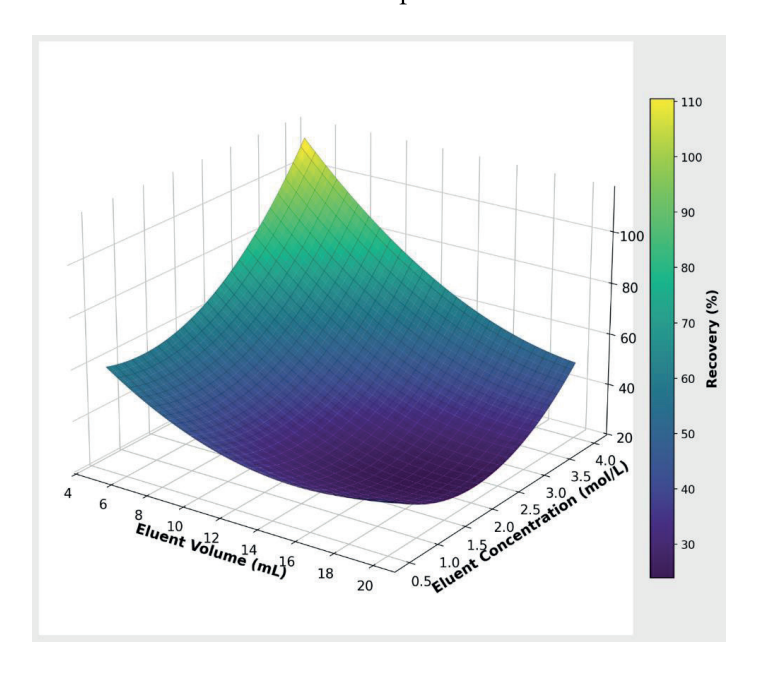


Fig.6. Effect of eluent volume and concentration on Zn(II) recovery in the elution process.

In the elution of Zn(II) from the AXAD-4 column, the effects of three independent variables, namely elution volume, concentration and flow rate, on recovery were investigated.

Figure 6 was obtained by comparing the flow rate and eluent volume while keeping the eluent concentration constant (4 mol/L). Eluent volume is clearly the most important variable. The recovery rate decreased where the eluent volume was high and increased where it was low. The effect of the flow rate is minimal in this graph.

Figure 7 examines the effects of concentration and flow rate while keeping the volume constant (5 ml). It is clear that both variables have various effects on the graph, but when the slopes are examined, it can be observed that the role of eluent concentration is slightly greater. Together with the results in Figure 6, it is quite clear that the least influential variable is the flow rate.

In Figure 8, where the flow rate, the least influential variable, is kept constant at approximately 1.178 mol/L, it can be seen that the effects of both concentration and volume are very similar. When the slopes are followed, the effect of volume appears to be slightly greater, but when the effect of noise is also taken into account, it is not clear which variable has a greater effect. However, it is clear that for high recovery values, both variables must be kept at relatively low values.

The values kept constant in the graphs are the optimum values that maximize the recovery value in the elution process, as in the sorption process. It was determined that the optimal elution conditions were as follows: a flow rate of 1.178, an eluent volume of 5 ml, and an eluent concentration of 4 mol/L. As a result of these variable values, the maximum recovery was found to be 112.99%.

4. Conclusions

Data science is now a highly researched area with applications in nearly every industry due to the exponential development in computing capacity that characterizes digital technology. Multivariate polynomial regression is one of the most basic and popular data science methods.

Using experimental data of the SPE method parameters developed for the preconcentration and separation of Zn(II) ions with AXAD-4 resin the Multivariate Polynomial Regression (MPR) Method was used in this study to determine the optimal SPE conditions that will maximize the sorption and elution capacity of the stationary phase.

In this study, the determination of Zn(II) ion using the SPE method on AXAD-4 resin was developed. The method involved the optimisation of independent variables such as pH, sample volume, sample and eluent flow rate, and eluent concentration. The ideal parameters for the sorption process were found to be a pH of 4.39 for the sample volume and a sample flow rate of 1000 mL, with a flow rate of 4 mLmin⁻¹. For the elution procedure, the ideal values were found to be 1.18 molL⁻¹ for the eluent concentration, 5 mL for the eluent volume and 4 mLmin⁻¹ for the elution flow rate. Following the implementation of the SPE method, analysis of Zn(II) was conducted by means of the UV-VIS spectrophotometric technique.

This method is both cost-effective and accessible, requiring no additional technical expertise. The present study employed MPR methodologies in order to ascertain the values that would demonstrate the highest recovery efficiency from the analytical data of the SPE method. The SPE method was developed using AXAD-4 resin for the sensitive and accurate analysis of very low levels of zinc in water samples.

Multivariate polynomial regression was applied to data sets of 15 clusters in order to characterise the independent variables in this study. Its scalability and applicability to larger data sets will contribute to other

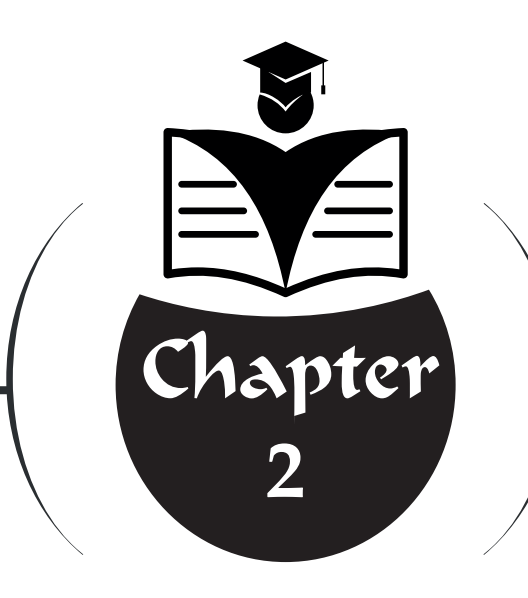
studies in this field. In conclusion, this study demonstrates that classical modelling methods could be employed effectively in analytical processes when combined with efficient optimisation techniques. The proposed method has the potential to offer an effective and practical solution to accurate and efficient optimization for heavy metal analysis.

REFERENCES

- Rezaee, M., & Tajer-Mohammad-Ghazvini, P. (2022). Rapid and efficient determination of zinc in water samples by graphite furnace atomic absorption spectrometry after homogeneous liquid-liquid microextraction via flotation assistance. *Bulletin of the Chemical Society of Ethiopia*, 36(1), 1-11.
- Al-Murshedi, A. Y., Shabaa, G. J., Azooz, E. A., Naguib, I. A., Haq, H. U., El Abbadi, N. K., & Snigur, D. (2025). Spectrophotometric determination of zinc in blood and food samples using an air-assisted rapid synergistic-cloud point extraction method based on deep eutectic solvents. *Journal of Food Composition and Analysis*, 137, 106910.
- Walther, U. I., Schulze, J., & Forth, W. (1998). Inhibition of protein synthesis by zinc: comparison between protein synthesis and RNA synthesis. *Human & experimental toxicology*, *17*(12), 661-667.
- Molenda, M., & Kolmas, J. (2023). The role of zinc in bone tissue health and regeneration—a review. *Biological trace element research*, *201*(12), 5640-5651.
- Umaz, K., Umaz, A., Aydin, I., & Aydin, F. (2025). Determination of zinc in dried nuts by slotted quartz tube-flame atomic absorption (SQT-FAAS) with citric acid-coated spectrometry magnetic nanoparticle (CAMNP) based solid phase extraction (SPE). *Instrumentation Science & Technology*, 53(1), 109-125.
- Haq, H. U., Balal, M., Castro-Muñoz, R., Hussain, Z., Safi, F., Ullah, S., & Boczkaj, G. (2021). Deep eutectic solvents based assay for extraction and determination of zinc in fish and eel samples using FAAS. *Journal of Molecular Liquids*, 333, 115930.
- Buszewski, B., & Szultka, M. (2012). Past, present, and future of solid phase extraction: a review. *Critical Reviews in Analytical Chemistry*, 42(3), 198-213.

- Ozdemir, S., Mohamedsaid, S. A., Kilinc, E., Yıldırım, A., & Soylak, M. (2018). Application of magnetized fungal solid phase extractor with Fe₂O₃ nanoparticle for determination and preconcentration of Co (II) and Hg (II) from natural water samples. *Microchemical Journal*, *143*, 198-204.
- Stafiej, A., & Pyrzynska, K. (2008). Solid phase extraction of metal ions using carbon nanotubes. *Microchemical Journal*, 89(1), 29-33.
- Mashhadizadeh, M. H., & Karami, Z. (2011). Solid phase extraction of trace amounts of Ag, Cd, Cu, and Zn in environmental samples using magnetic nanoparticles coated by 3-(trimethoxysilyl)-1-propantiol and modified with 2-amino-5-mercapto-1, 3, 4-thiadiazole and their determination by ICP-OES. *Journal of Hazardous Materials*, 190(1-3), 1023-1029.
- Shemirani, F., Mirroshandel, A. A., Salavati Niasari, M., & Rahnama Kozani, R. (2004). Silica gel coated with Schiff's base: Synthesis and application as an adsorbent for cadmium, copper, zinc, and nickel determination after preconcentration by flame atomic absorption spectrometry. *Journal of Analytical Chemistry*, *59*(3), 228-233.
- Saxena, R., & Meena, P. L. (2014). Flow injection online solid phase extraction system using Amberlite XAD-16 functionalized with 8-hydroxyquinoline for copper and zinc determination by flame atomic absorption spectrometry. *RSC Advances*, 4(39), 20216-20225.
- Ozdemir, S., Kılınç, E., Acer, Ö., & Soylak, M. (2022). Preconcentrations of Zn (II) and Hg (II) in environmental and food samples by SPE on B. licheniformis loaded Amberlite XAD-4. *Biological Trace Element Research*, 200(4), 1972-1980.
- Zawierucha, I., Kozlowska, J., Kozlowski, C., & Trochimczuk, A. (2014). Sorption of Pb (II), Cd (II) and Zn (II) performed with the use of carboxyphenylresorcinarene-impregnated Amberlite XAD-4 resin. *Desalination and Water Treatment*, *52*(1-3), 314-323.

- Ahmad, A., Siddique, J. A., Laskar, M. A., Kumar, R., Mohd-Setapar, S. H., Khatoon, A., & Shiekh, R. A. (2015). New generation Amberlite XAD resin for the removal of metal ions: A review. *Journal of Environmental Sciences*, *31*, 104-123.
- Sarker, I. H. (2021). Data science and analytics: an overview from datadriven smart computing, decision-making and applications perspective. *SN Computer Science*, *2*(5), 377.
- Cai, X., Langtangen, H. P., & Moe, H. (2005). On the performance of the Python programming language for serial and parallel scientific computations. *Scientific Programming*, *13*(1), 31-56.
- Su, M., Zhong, Q., & Peng, H. (2021). Regularized multivariate polynomial regression analysis of the compressive strength of slag-metakaolin geopolymer pastes based on experimental data. *Construction and building materials*, 303, 124529.
- Paradkar, R. P., & Williams, R. R. (1994). Micellar colorimetric determination of dithizone metal chelates. *Analytical chemistry*, 66(17), 2752-2756.
- Sinha, P. (2013). Multivariate polynomial regression in data mining: methodology, problems and solutions. Int. J. Sci. Eng. Res, 4(12), 962-965.
- Hastie, T., Tibshirani, R., Friedman, J., & Friedman, J. H. (2009). Springer series in statistics the elements of statistical learning. *Math. Intell*, *27*(2), 83-85.
- Montgomery, D. C., Peck, E. A., & Vining, G. G. (2021). *Introduction to linear regression analysis*. John Wiley & Sons.



INVESTIGATION OF THE ANTIBACTERIAL ACTIVITY OF THE CONTEZOLID MOLECULE USING IN SILICO METHODS: DFT AND MOLECULAR DOCKING STUDIES





Emel EKİNCİ¹ Özlem GÜNDOĞDU AYTAÇ² Sertan AYTAÇ³

¹ Lecturer Dr., Çankırı Karatekin University, Central Research Laboratory Application and Research Center, Çankırı, Türkiye. Orcid ID: 0000-0003-2323-2747

² Assoc. Prof. Dr., Kırşehir Ahi Evran University, Kaman Vocational School, Food Processing Department, Kaman-Kırşehir, Türkiye. Orcid ID: 0000-0002-6943-9674 3 Assist. Prof. Dr., Kırşehir Ahi Evran University, Kaman Vocational School, Food Processing Department, Kaman-Kırşehir, Türkiye. Orcid ID: 0000-0002-3196-4545

INTRODUCTION

Antibiotics are widely used agents in the prevention and treatment of bacterial infections. However, the increasing antibiotic resistance in recent years has posed significant challenges in managing infectious diseases (Nwobodo et al., 2022). The spread of resistant bacterial strains reduces the effectiveness of current antibacterial treatment options and necessitates the development of stronger and more innovative antibiotics (Belay et al., 2024). In this context, the chemical building blocks used in the design of new antibiotics hold great importance in terms of specificity to biological targets, pharmacokinetic properties, and toxicological safety (Breijyeh & Karaman, 2023).

Heterocyclic compounds are organic molecules that contain ring structures with heteroatoms such as nitrogen (N), oxygen (O), or sulfur (S) in addition to carbon atoms. These structures serve as fundamental components in the synthesis of numerous products, including pharmaceuticals, agrochemicals, disinfectants, antioxidants, copolymers, corrosion inhibitors, and dyes (Qadir et al., 2022; Hamad, 2025). Due to their presence in biologically active molecules, heterocyclic rings are highly valuable in drug research (Poturcu & Çubuk Demiralay, 2019). Both natural and synthetic forms of these compounds form the core structures of essential biomolecules such as vitamins, hormones, and antibiotics (Prasad & Patel, 2024). In particular, nitrogen-containing heterocyclic compounds are regarded as indispensable chemical scaffolds in modern drug design (Taylor et al., 2016).

The heterocyclic rings present in the structural framework of antibiotics play a decisive role in their pharmacological activity. Through specific interactions with biological targets, they enhance therapeutic efficacy (Shivaji & Kasabe, 2021). Such rings are also found in the fundamental structures of antibiotics like penicillin (Sabah, 2014), cephalosporin (Breijyeh & Karaman, 2023), rifampicin (Hardie & Fenn, 2022), and tetracycline (Tariq et al., 2018) (Figure 1).

Figure 1. Some important antibiotics and their skeletal structures

Compounds containing heteroatoms such as nitrogen (N), sulfur (S), and oxygen (O) in five- and six-membered rings play a central role in medicinal

chemistry (Sharma et al., 2015). Among these compounds, oxazolidinones are notable for their five-membered rings that include both nitrogen and oxygen atoms (Foti et al., 2021). Oxazolidinones possess a distinct structure compared to other antibacterial agents and are considered a new class of synthetic antibiotics (Malik et al., 2023). Depending on the position of the heteroatoms within the ring, different isomers exist, namely 2-, 3-, and 4-oxazolidinones (Fernandes et al., 2023) (Figure 2). Among these isomers, the 2-oxazolidinone core is particularly critical for antibacterial activity (Li et al., 2023).

O

$$3$$
 \parallel^2 \parallel^2 \parallel^3 \parallel^4 \parallel^3 \parallel^4 \parallel^5 \parallel^5 \parallel^2 \parallel^3 \parallel^4 \parallel^5 \parallel^5 \parallel^2

Figure 2. Isomeric structures of oxazolidinones

Structurally, the oxazolidinone ring contains a side group with an S stereoconfiguration at the C5 position and a phenyl ring attached to the N3 position (Mahdi et al., 2023). In terms of mechanism of action, these compounds inhibit protein synthesis by binding to the bacterial 50S ribosomal subunit and the peptidyl transferase center (PTC). This mechanism disrupts vital bacterial processes, thereby exerting an antimicrobial effect (Malik et al., 2023).

Oxazolidinones exhibit potent antimicrobial activity, particularly against methicillin-resistant *Staphylococcus aureus* (MRSA), vancomycin-resistant enterococci (VRE), and other multidrug-resistant (MDR) Gram-positive pathogens (Wang et al., 2025). The first oxazolidinone derivatives were developed in 1978 for use against plant pathogens. Later, in 1987, DuP-105 and DuP-721 were synthesized for human pathogens; however, they were withdrawn from clinical development due to toxicity concerns. With the resolution of these issues, derivatives such as linezolid and eperezolid, which showed reduced toxicity levels, were developed in 1996 (Bozdogan & Appelbaum, 2004; Rani et al., 2021).

Linezolid and eperezolid, which were approved by the United States Food and Drug Administration (FDA), have demonstrated efficacy against MRSA, VRE, streptococci, and other Gram-positive bacteria (Xu et al., 2008; Roger et al., 2018). However, these agents do not exhibit significant activity against Gram-negative bacteria (Edlund et al., 1999). Additionally, although in vitro activity has been observed against certain anaerobic bacteria, their clinical efficacy against these organisms remains limited (Karakök et al., 2019; Liu et al., 2020) (Figure 3).

Figure 3. Some oxazolidinone compounds

In addition to linezolid and eperezolid, many new molecules have also been developed within the oxazolidinone class. These include sutezolid, delpazolid, tedizolid, radezolid, posizolid, TBI-223, and Contezolid (Mahdi et al., 2023; Chen et al., 2024) (Figure 4). These compounds exhibit strong antimicrobial activity by effectively inhibiting bacterial protein synthesis (Pathania et al., 2023).

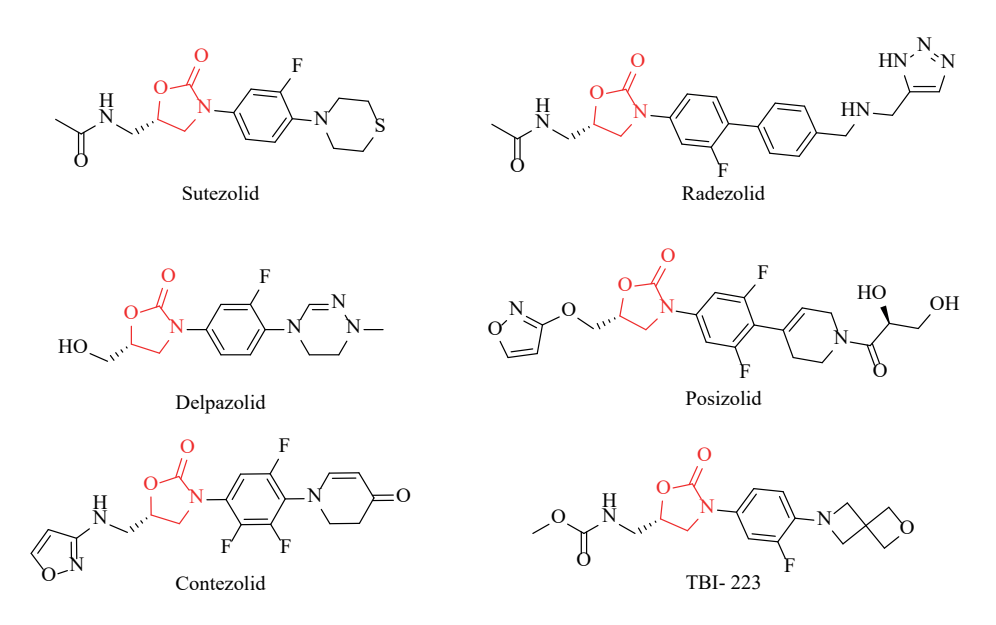


Figure 4. Some developed oxazolidinone derivative compounds

Delpazolid is effective against pathogens such as MRSA, VRE, and Mycobacterium tuberculosis (Cho and Jang, 2020). Sutezolid, developed as a thiomorpholinyl derivative of linezolid, has shown higher efficacy against infections caused by M. tuberculosis (Kiran et al., 2025). Tedizolid is effective against many Gram-positive bacteria, including MRSA and VRE, and is used in the treatment of skin and soft tissue infections (Iqbal et al., 2022). Radezolid,

one of the next-generation oxazolidinones, has been approved by the FDA for clinical trials and has attracted attention for its strong antibacterial activity (Wang et al., 2023). Still under development, posizolid is considered a potential agent against Gram-positive bacteria such as *Staphylococcus, Enterococcus, and Streptococcus pneumoniae* (Wookey et al., 2004; Almalki et al., 2022). Similarly, TBI-223 shows linezolid-like efficacy against tuberculosis but presents a safer profile in terms of bone marrow and nervous system toxicities (Strydom et al., 2024; Lombardi et al., 2025).

Contezolid, one of the new-generation oxazolidinones, has undergone chemical modifications to offer a lower toxicity profile and emerges as a more effective solution against antibiotic resistance. Compared to linezolid, it has been reported to show a lower level of serotonergic neurotoxicity associated with monoamine oxidase (MAO) activity (Wang et al., 2021). Additionally, experimental studies in mice have revealed that Contezolid induces less myelosuppression than linezolid (Wei et al., 2025). In vitro studies have also demonstrated that Contezolid is effective against multidrug-resistant bacteria such as MRSA and VRE (Carvalhaes et al., 2020). Due to the 2-oxazolidinone ring in its structure, Contezolid inhibits bacterial protein synthesis (Zhang et al., 2024). This effect is achieved by binding to the 23S rRNA of the bacterial 50S ribosomal subunit, thereby blocking the entry of aminoacyl-tRNA and halting bacterial growth (Brenciani et al., 2022).

Understanding the antibacterial activity and molecular interactions of the Contezolid molecule is of significant importance for the development of next-generation antibiotics. In this context, the present study investigates the potential effects of Contezolid on bacterial enzyme targets using in silico methods. Specifically, molecular docking analyses were performed to evaluate the interaction of Contezolid with DNA gyrase B (GyrB) enzymes from *Staphylococcus aureus* (PDB ID: 6TTG) and *Escherichia coli* (PDB ID: 4DUH). Norfloxacin, a widely used clinical antibiotic targeting similar bacterial enzymes, was used as a reference compound for comparative purposes.

In addition to the docking studies, the electronic and structural properties of Contezolid, which play a key role in its biological activity, were examined in detail. For this purpose, density functional theory (DFT) approaches were employed to calculate global reactivity parameters, determine the HOMO–LUMO energy gap, and generate a molecular electrostatic potential (MEP) map. The results obtained from these analyses aim to provide a deeper understanding of Contezolid's interaction mechanisms with bacterial targets and contribute valuable insights into its potential as a candidate for future antibiotic development.

Material and Method

Global reactivity descriptors

The molecular geometry was optimized, and the harmonic vibrational frequencies were calculated using the density functional theory method with the B3LYP functional (Becke, 1993; Lee et al., 1988) and the 6-311++(d, p) basis set (Frisch, 1984). To gain a better understanding of the chemical reactivity and kinetic stability of the molecules, global reactivity parameters were evaluated as key quantum chemical descriptors. These values offer insight into the electronic properties of the molecules and their potential interactions with biological receptors. All quantum chemical calculations were performed using the Gaussian 16 software.

Molecular Docking Studies

Molecular docking is a widely used computational method in drug discovery and pharmacology that enables the prediction of protein-ligand interactions and the identification of potential binding sites with high accuracy and efficiency (Gündoğdu Aytaç et al., 2025; Mahmudov et al., 2022). In this study, *Staphylococcus aureus* GyrB (PDB ID: 6TTG) and *Escherichia coli* DNA gyrase B (PDB ID: 4DUH) were selected as target proteins for in silico docking experiments (Shah et al., 2025). Contezolid was evaluated as the test compound, while Norfloxacin was used as the reference drug for comparative purposes (Elumalai et al., 2024).

The 3D structures of Contezolid and Norfloxacin were generated by first drawing their 2D chemical structures, followed by geometry optimization using the Avogadro software. Protein structures were obtained from the Protein Data Bank (https://www.rcsb.org/). Ligand and protein preparations were carried out using MGLTools, where water molecules were removed, polar hydrogens were added, and Kollman charges were assigned. The torsional flexibility of the ligands was defined, and all molecules were saved in PDBQT format for docking.

To ensure accurate binding predictions, the active sites of the proteins were defined, and grid box parameters were carefully set. For *S. aureus* GyrB (PDB ID: 6TTG), the grid dimensions were $60 \times 60 \times 60 \times 60$ ų, with a spacing of 0.553 Å, and center coordinates at x = 6.805, y = 2.238, and z = -0.835. For *E. coli* DNA gyrase B (PDB ID: 4DUH), the grid center was set at x = 30.654, y = 4.821, and z = 4.880, using the same spacing.

Molecular docking simulations were performed using AutoDock 1.5.7 with the Lamarckian Genetic Algorithm (LGA) protocol. This method allowed for the evaluation of key non-covalent interactions, including hydrogen bonds, van der Waals forces, and hydrophobic contacts between the ligands and their respective binding sites.

The resulting protein-ligand complexes were visualized and analyzed using BIOVIA Discovery Studio to examine binding poses and interaction profiles. Docking scores and interaction diagrams are presented in Tables 2–6 and Figures 8–11, providing insights into the potential antibacterial activity of Contezolid compared to the reference drug.

RESULTS and DISCUSSION

Molecular Geometry

Geometric optimization of the Contezolid molecule was performed using the DFT method using the B3LYP functional and the 6-311++G(d,p) basis set. As a result of the optimization, the stable structure with the minimum energy of the molecule was determined, which formed the basis of subsequent electronic property analyses, molecular orbital calculations, and docking studies.

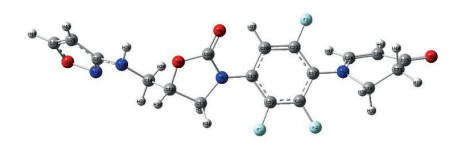


Figure 5. *3D structure of the Contezolid molecule*

Global reactivity descriptors

The quantum chemical parameters obtained for the Contezolid molecule provide important insights into its electronic structure and reactivity. The values of these parameters for Contezolid are presented in Table 1.

Parameters	Values
E _{HOMO} (eV)	-0.299
$E_{LUMO}(eV)$	-0.198
Energy gap E _{HOMO} - E _{LUMO}	0.102
Ionization potential $(I = -E_{HOMO})$	0.299
Electron affinity ($A = -E_{LUMO}$)	0.198
Chemical hardness ($\eta = (I - A)/2$)	0.051
Chemical softness ($\sigma = 1/\eta$)	19.68
Electronegativity ($\chi = (I+A)/2$)	0.248
Chemical potential ($\mu = -(I+A)/2$)	-0.248
Electrophilicity ($\omega = \mu 2/2n$)	0.607

Table 1. Global reactivity parameters in (eV) for Contezolid

The HOMO and LUMO energy levels were calculated to be –0.299 eV and –0.198 eV, respectively, with a relatively small energy gap between them ($\Delta E=$

0.102 eV), as shown in Figure 6. This narrow gap indicates that the molecule is highly reactive and possesses good electron conductivity. The ionization potential (0.299 eV) and electron affinity (0.198 eV) values suggest that Contezolid has the ability to both donate and accept electrons. The molecule exhibits low chemical hardness (= 0.051 eV) and high chemical softness (σ = 19.68), reflecting a structure that is easily polarizable and chemically reactive. Its electronegativity (χ = 0.248 eV) and chemical potential (μ = -0.248 eV) indicate a tendency to attract electrons. The electrophilicity index (ω = 0.607 eV) points to a moderate electrophilic nature. Taken together, these findings suggest that Contezolid is a soft, reactive compound with a strong potential for interactions within biological environments.

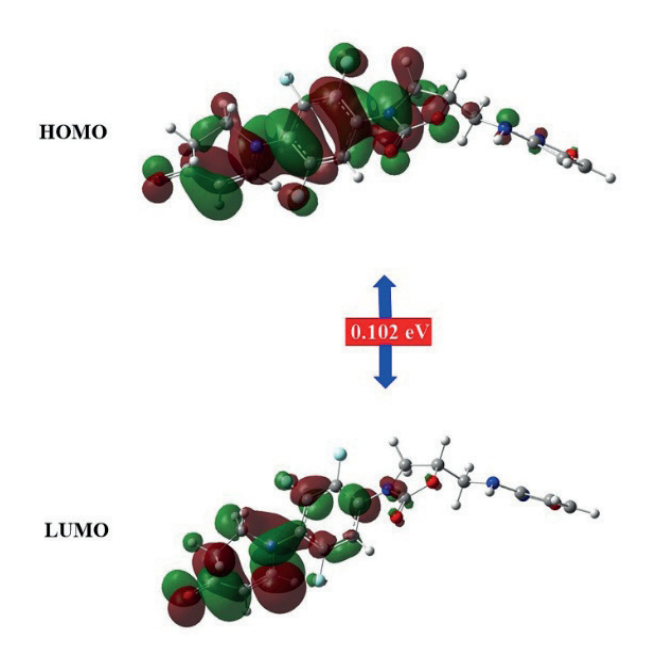


Figure 6. The FMOs of Contezolid obtained at the B3LYP/6-311++(d, p) level.

Molecular Electrostatic Potential (MEP) Maps

Molecular electrostatic potential (MEP) maps help predict a molecule's reactivity by visualizing the charge distribution on its three-dimensional molecular surface (Murray et al., 2011). These maps illustrate the spatial distribution of electrostatic charges across the molecule, highlighting areas of electron density and partial charges (Madalambika et. al., 2025). The color variations on the MEP surface indicate different levels of electrostatic potential: red areas typically represent electron-rich regions (negative potential), while blue areas correspond to electron-deficient regions (positive potential) (Frisch, et al. 2016; El-Sayed et. al, 2025).

In the case of Contezolid, the red-shaded regions on the MEP map are concentrated around the oxygen atoms. This suggests that these areas are prone to nucleophilic attack and may act as hydrogen bond acceptor sites. In contrast, the blue-shaded areas usually indicate regions with electrophilic character or proton-donating ability, particularly around nitrogen atoms and amine groups. This distribution shows that Contezolid contains both electron-rich and electron-poor zones within the same structure, pointing to an electronically polar nature (Figure 7).

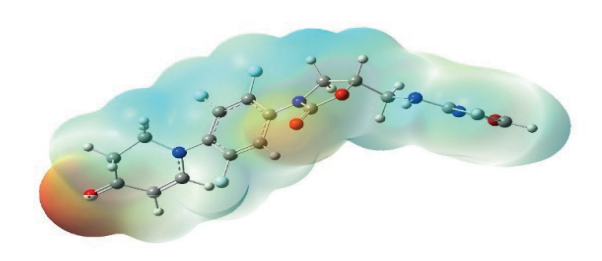


Figure 7. Molecular electrostatic potential (MEP) map of Contezolid obtained at the B3LYP/6-311++(d,p) level.

Overall, the electrostatic potential surface of Contezolid reveals a heterogeneous charge distribution, indicating that the molecule is well-suited for hydrogen bonding interactions. This characteristic enables the compound to form strong electrostatic interactions with biological targets—particularly with active sites that contain polar or charged amino acid residues. Consequently, the MEP analysis supports the idea that Contezolid possesses high electrostatic compatibility and a strong potential for active site recognition, both of which contribute to its pharmacological effectiveness.

Molecular Docking Studies

In this study, molecular docking analyses were performed to compare the antibacterial properties of Contezolid with those of the reference drug Norfloxacin. For the docking simulations, *Staphylococcus aureus* GyrB protein (PDB ID: 6TTG) and *Escherichia coli* DNA gyrase B protein (PDB ID: 4DUH) were selected as target proteins (Shah et al., 2025). Norfloxacin was used as the standard reference drug for comparative evaluation (Elumalai et al., 2024). The docking results for the compounds are presented in Tables 2–6.

Interaction analysis of Contezolid at the active site of the target protein (4DUH) revealed the formation of several conventional hydrogen bonds with

ARG76 (2.28 Å) and ARG136 (2.54 Å). A π -cation interaction was observed with LYS103 (4.26 Å), and a π -anion interaction was detected with GLU50 (4.22 Å). Additionally, π -alkyl interactions were found with LYS103 (4.58 Å) and ILE78 (4.52 Å). Halogen bonding interactions were identified with GLY77 (3.56 Å) and ASN46 (3.64 Å). Furthermore, van der Waals interactions were observed with several residues, including PRO79, GLY102, GLY101, ILE94, VAL167, VAL43, ASP73, THR165, and ALA47 (Figure 8). All molecular interactions are detailed in Table 2.

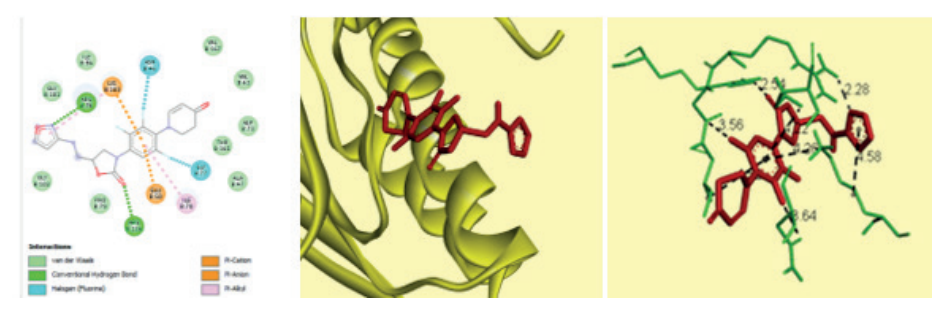


Figure 8. Docking interactions between the protein 4DUH and the Contezolid **Table 2.** Protein-ligand interaction binding energy of the Contezolid with 4DUH

Compound	Interaction Type	Residues	Distance	Binding Energy Kcal/Mol
	Conventional Hydrogen Bond	ARG76	2.28	-6.81
		ARG136	2.54	
	π-Cation	LYS103	4.26	
F F O	π-Anion	GLU50	4.22	
	π-Alkyl	LYS103	4.58	
		ILE78	4.52	
Condezolid	Halagan E	GLY77	3.56	
	Halogen- F-	ASN46	3.64	
	Van der Waals	PRO79, GLY102, GLY101, ILE94, VAL167,		
	van der waais	VAL43, ASP73, THR165, ALA47		

The interaction analysis of the Contezolid within the active site of the target protein (6TTG) revealed the presence of multiple conventional hydrogen bonds formed with residues GLY85 (1.79 Å) and ASN54 (2.12 and 1.98 Å). In addition, π -anion and π -sigma interactions were observed with residue GLU50 (3.73 and 3.99 Å) respectively. π -alkyl interactions were also detected with residues VAL131 (4.97 Å), ILE86 (4.70 Å), and ILE102 (5.34 Å). Furthermore, van der Waals interactions were found to occur with residues VAL130, SER129, ILE51, LEU103, SER55, THR173, ASP81, GLY83, GLY172, ARG84, and GLU58 (Figure 9). All molecular interactions are detailed in Table 3.

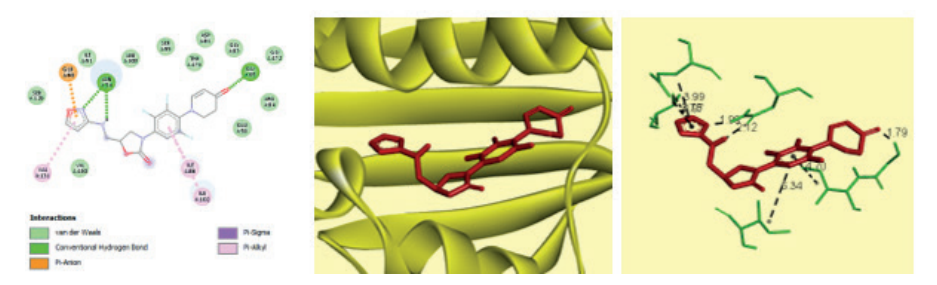


Figure 9. *Docking interactions between the protein 6TTG and the Contezolid*

Table 3. Protein-ligand interaction binding energy of the Contezolid with 6TTG

Compound	Interaction Type	Residues	Distance	Binding Energy Kcal/ Mol	
	Conventional Hydrogen Bond	GLY85	1.79		
		ASN54	2.12		
		ASN54	1.98		
	π-Anion	GLU50	3.73	-7.47	
F F O	π-Sigma	GLU50	3.99	-/.4/	
		VAL131	4.97		
F Condezolid	π-Alkyl	ILE86	4.70		
Condezond		ILE102	5.34		
	Van der Waals	VAL130, SER129, ILE51, LEU103, SER55, THR173, ASP81, GLY83, GLY172, ARG84, GLU58			

The interaction analysis of the Norfloxacin within the active site of the target protein revealed a the presence of multiple conventional hydrogen bonds were formed with residues ASP49 (2.26 Å), HIS99 (2.39 and 3.07 Å), ALA100 (2.28 Å), and SER121 (2.03 Å). In addition, carbon hydrogen bonds were observed with residues ALA100 (3.21 Å), HIS99 (3.15 Å), GLY117 (3.39 Å), LYS103 (2.81 Å), ASN46 (2.89 and 3.74 Å), and ASP45 (3.45 Å). π -anion interaction was detected with residue GLU42 (4.99 Å), while alkyl interactions were observed with residue LYS103 (4.18 and 3.99 Å). Moreover, a π -alkyl interaction was found with residue LYS103 (4.77 Å), and a halogen (fluorine) bond was identified with residue GLY117 (3.39 Å). Furthermore, van der Waals interactions were detected with residues LEU98, VAL120, VAL97, ILE94, GLY101, PHE104, GLY119, VAL118, and VAL122 (Figure 10). All molecular interactions are detailed in Table 4.

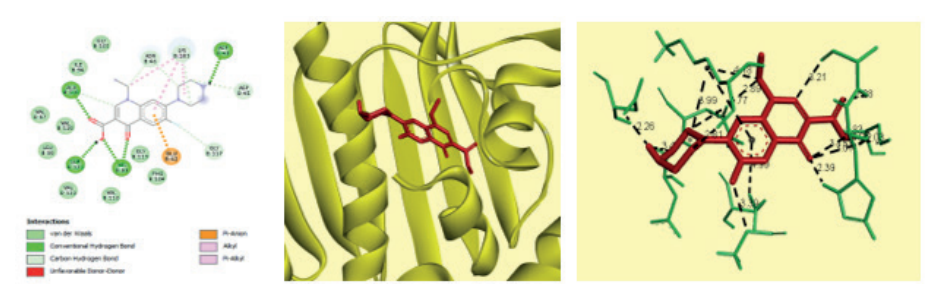


Figure 10. Docking interactions between the protein 4DUH and the Norfloxacin **Table 4.** Protein-ligand interaction binding energy of the Norfloxacin with 4DUH

Compound	Interaction Type	Residues	Distance	Binding Energy Kcal/ Mol
	Conventional Hydrogen Bond	ASP49	2.26	-7.02
		HIS99	2.39	
		HIS99	3.07	
		ALA100	2.28	
		SER121	2.03	
	Carbon Hydrogen Bond	HIS99	3.15	
0 0		ALA100	3.21	
F, A, J, J, J, J, J, J, J, J, J, J, J, J, J,		GLY117	3.39	
ОН		LYS103	2.81	
N N		ASN46	2.89	
HŇ		ASN46	3.74	
Norfloxacin		ASP45	3.45	
	π-Anion	GLU42	4.99	
	4.11 1	LYS103	4.18	
	Alkyl	LYS103	3.99	
	π-Alkyl Halogen- F-	LYS103	4.77	
		GLY117	3.39	
	Van der Waals	LEU98, VAL120, VAL97, ILE94, GLY101, PHE104, GLY119, VAL118, VAL122		

The interaction analysis of Norfloxacin within the active site of the target protein revealed the presence of multiple conventional hydrogen bonds were formed with residues THR173 (2.72 Å) and ARG84 (2.92 Å). Additionally, π -cation interaction was detected with residue ARG84 (4.71 Å), while π -anion interactions were identified with residue GLU58 (4.04 and 4.50 Å). Alkyl interactions were formed with residues ILE102 (5.08 Å) and ILE86 (5.29 Å), and π -sigma interactions were observed with residues ILE86 (3.98 Å) and PRO87 (3.91 Å). Moreover, π -alkyl interaction was found with residue ILE86 (4.34 Å). Halogen (fluorine) bonds were also detected with residues THR173 (2.72 Å) and ASP81 (2.71 and 2.95 Å). Furthermore, van der Waals interactions occurred with residues GLY83, GLY85, ARG144, SER55, ILE51, ILE175, ASN54 and LEU103 (Figure 11). All molecular interactions are detailed in Table 5.

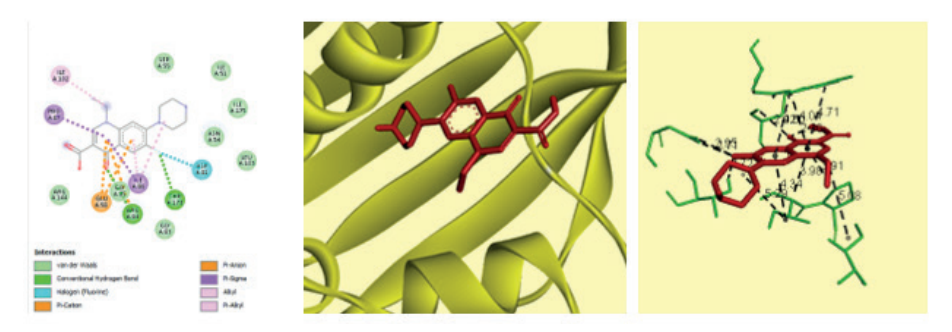


Figure 11. Docking interactions between the protein 6TTG and the Norfloxacin **Table 5**. Protein-ligand interaction binding energy of the Norfloxacin with 6TTG

Compound	Interaction Type	Residues	Distance	Binding Energy Kcal/Mol
	Conventional Hydrogen Bond	THR173	2.72	-6.76
		ARG84	2.92	
	π-Cation	ARG84	4.71	
	π-Anion	GLU58	4.04	
		GLU58	4.50	
0 0	Alkyl	ILE102	5.08	
FOH		ILE86	5.29	
N	π-Sigma	ILE86	3.98	
HN		PRO87	3.91	
Norfloxacin	π-Alkyl	ILE86	4.34	
	Halogen- F-	THR173	2.72	
		ASP81	2.71	
		ASP81	2.95	
	Van der Waals GLY83, GLY85, ARG144, SER55			44, SER55,
	vali uel vvaals	ILE51, ILE175, ASN54, LEU103		

Table 6 presents the lowest binding energies, RMSD values, and estimated inhibition constants (Ki) obtained from molecular docking studies of Contezolid and Norfloxacin with the 4DUH and 6TTG proteins. These results were used to assess and compare the binding affinities of both compounds to their respective target proteins.

For Contezolid, the lowest binding energy against the 6TTG protein was calculated as –7.47 kcal/mol, indicating a strong binding interaction. The estimated $K_{_{\rm i}}$ for this interaction was 3.37 μM , suggesting a high inhibitory potential. In contrast, docking results with the 4DUH protein showed a binding energy of –6.81 kcal/mol and a Ki value of 10.12 μM , indicating a comparatively weaker interaction than with 6TTG. In the case of Norfloxacin, the lowest binding energy was –7.02 kcal/mol with the 4DUH protein, accompanied by a Ki value

of 7.19 μ M, reflecting a moderate level of inhibition. Against the 6TTG protein, Norfloxacin exhibited a binding energy of –6.76 kcal/mol and a Ki of 11.11 μ M, suggesting a relatively weaker interaction. When examining the RMSD values, lower values were observed in the docking studies involving the 6TTG protein. This indicates that the ligand conformations were closer to the reference structure and that the interactions were likely more stable in those complexes. Overall, Contezolid demonstrated stronger binding affinity and higher inhibitory potential than Norfloxacin, as evidenced by its lower binding energies and smaller K_i values across both target proteins. These findings support the potential of Contezolid as an effective inhibitor for the studied bacterial targets.

Compound	Protein	Lowest Binding Energy (kcal/ mol)	Reference RMDS	Estimated Ki (µM)
C41: 1	4DUH	-6.81	25.33	10.12 uM
Contezolid	6TTG	-7.47	9.62	3.37
Norfloxacin	4DUH	-7.02	33.75	7.19
	6TTG	-6.76	6.41	11.11

Table 6. Docking results of Contezolid and Norfloxacin

Conclusion

In conclusion, the in silico analyses conducted in this study have revealed the broad-spectrum antibacterial potential of Contezolid. DFT (Density Functional Theory) simulations provided valuable insights into the molecule's electronic properties and potential interaction sites. In particular, global reactivity parameters, HOMO-LUMO energy levels, and molecular electrostatic potential (MEP) maps offered fundamental information for understanding Contezolid's interactions with biological targets. Additionally, molecular docking studies were performed to comparatively assess the binding affinities of Contezolid and Norfloxacin to E. coli DNA gyrase B (PDB ID: 4DUH) and S. aureus GyrB (PDB ID: 6TTG) proteins. The results demonstrated that Contezolid exhibited strong interaction with S. aureus GyrB, indicated by a binding energy of -7.47 kcal/mol. Conversely, Norfloxacin showed effective binding to E. coli DNA gyrase B, with a binding energy of -7.02 kcal/mol. Overall, although both compounds were able to interact with both target proteins, the findings suggest that Contezolid possesses higher inhibitory potential against gram-positive bacteria, particularly S. aureus, whereas Norfloxacin appears to be more effective against gram-negative bacteria such as E. coli. Based on these observations, Contezolid emerges as a promising antibacterial agent, especially for the treatment of infections caused by grampositive pathogens.

REFERENCES

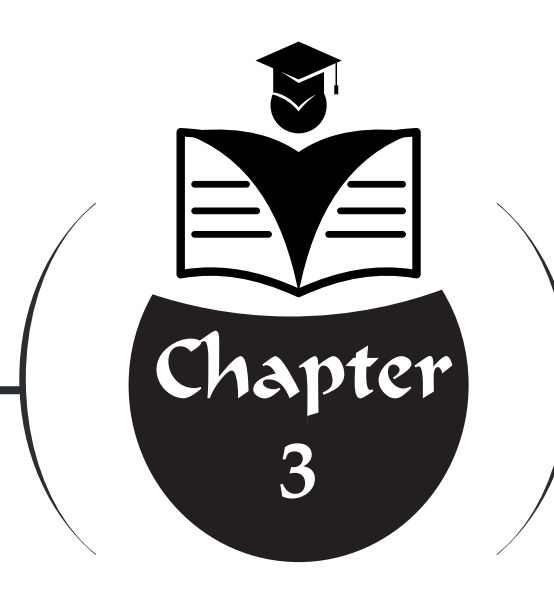
- Almalki, A. J., Ibrahim, T. S., Taher, E. S., Mohamed, M. F. A., Youns, M., Hegazy, W. A. H., & Al-Mahmoudy, A. M. M. (2022). Synthesis, antimicrobial, anti-virulence and anticancer evaluation of new 5(4H)-oxazolone-based sulfonamides. *Molecules*, *27*(3), 671. https://doi.org/10.3390/molecules27030671
- Becke, A. D. (1993). Density-functional thermochemistry. III. The role of exact exchange. *The Journal of Chemical Physics*, 98(7), 5648–5652. https://doi.org/10.1063/1.464913
- Belay, W. Y., Getachew, M., Tegegne, B. A., Teffera, Z. H., Dagne, A., Zeleke, T. K., ... & Aschale, Y. (2024). Mechanism of antibacterial resistance, strategies and next-generation antimicrobials to contain antimicrobial resistance: A review. *Frontiers in Pharmacology*, 15, 1444781. https://doi.org/10.3389/fp-har.2024.1444781
- Bozdogan, B., & Appelbaum, P. C. (2004). Oxazolidinones: Activity, mode of action, and mechanism of resistance. *International Journal of Antimicrobial Agents*, 23(2), 113–119. https://doi.org/10.1016/j.ijantimicag.2003.11.003
- Breijyeh, Z., & Karaman, R. (2023). Design and synthesis of novel antimicrobial agents. *Antibiotics*, 12(3), 628. https://doi.org/10.3390/antibiotics12030628
- Brenciani, A., Morroni, G., Schwarz, S., & Giovanetti, E. (2022). Oxazolidinones: Mechanisms of resistance and mobile genetic elements involved. *Journal of Antimicrobial Chemotherapy*, 77(10), 2596–2621. https://doi.org/10.1093/jac/dkac263
- Carvalhaes, C. G., Duncan, L. R., Wang, W., & Sader, H. S. (2020). In vitro activity and potency of the novel oxazolidinone Contezolid (MRX-I) tested against Gram-positive clinical isolates from the United States and Europe. *Antimicrobial Agents and Chemotherapy*, 64(11), e01195-20. https://doi.org/10.1128/AAC.01195-20
- Cho, Y. L., & Jang, J. (2020). Development of delpazolid for the treatment of tuberculosis. *Applied Sciences*, 10(7), 2211. https://doi.org/10.3390/app10072211
- El-Sayed, D. S., Abd-Elfatah, N. M., Khalil, T. E., Attia, A. A., & El-Dissouky, A. (2025). Synthesis, characterization, molecular docking, spectroscopic analysis, and computational studies of chloranilic acid–gemifloxacin charge transfer complex. *Journal of Molecular Structure*, *1348* (Part 1), 143372. https://doi.org/10.1016/j.molstruc.2025.143372
- Elumalai, K., Shanmugam, A., Devaraji, M., & Srinivasan, S. (2024). Synthesis and molecular docking of pyrimidine derivatives as antibacterial agents. *Carbon Resources Conversion*, 7, 100222. https://doi.org/10.1016/j.crcon.2024.100222
- Fernandes, G. F. S., Scarim, C. B., Kim, S.-H., Wu, J., & Castagnolo, D. (2023). Oxazolidinones as versatile scaffolds in medicinal chemistry. *RSC Medicinal Chemistry*, *14*, 823–847. https://doi.org/10.1039/D2MD00415A

- Foti, C., Piperno, A., Scala, A., & Giuffrè, O. (2021). Oxazolidinone antibiotics: Chemical, biological and analytical aspects. *Molecules*, 26(14), 4280. https://doi.org/10.3390/molecules26144280
- Frisch, M. J., et al. (2016). Gaussian 09 (Revision A.02). Gaussian, Inc., Wallingford, CT.
- Frisch, M. J., Pople, J. A., & Binkley, J. S. (1984). Self-consistent molecular orbital methods. 25. Supplementary functions for Gaussian basis sets. *The Journal of Chemical Physics*, 80(7), 3265–3269. https://doi.org/10.1063/1.447079
- Gündoğdu Aytaç, Ö., Gündoğdu, H. B., Aytaç, S., Bingöl, Z., Gülçin, İ., & Kara, Y. (2025). Novel isoindole-1,3-dione-isoxazole hybrids: Synthesis, characterization, evaluation of their inhibitory activities on carbonic anhydrase and acetylcholinesterase. *Journal of Biochemical and Molecular Toxicology*, 39(10), e70550. https://doi.org/10.1002/jbt.70550
- Hamad, H. T. (2025). The anti-cancer effectiveness of some heterocyclic compounds containing sulfur atom. *Results in Chemistry*, 15, 102182. https://doi.org/10.1016/j.rechem.2025.102182
- Hardie, K. R., & Fenn, S. J. (2022). JMM profile: Rifampicin: A broad-spectrum antibiotic. *Journal of Medical Microbiology*, 71, Article 001566. https://doi.org/10.1099/jmm.0.001566
- Iqbal, K., Milioudi, A., & Wicha, S. G. (2022). Pharmacokinetics and pharmacodynamics of tedizolid. *Clinical Pharmacokinetics*, 61(5), 489–503. https://doi.org/10.1007/s40262-021-01099-7
- Karakök, T., Kınıklı, S., & Cesur, S. (2019). Dirençli Gram pozitif bakteriyel enfeksiyonlarında kullanılan oksazolidinon grubu bir antibiyotik: Linezolid. *Anadolu Güncel Tıp Dergisi*, 1(1), 14–17.
- Kiran, G. U., Kumar, L. P., Mahesh, M., Manikanta, K. U. S., Nehemiah, G., & Kumar, G. P. (2025). Sutezolid: A promising next generation tuberculosis agent. *World Journal of Biology Pharmacy and Health Sciences*, 23(2), 348–355. https://doi.org/10.30574/wjbphs.2025.23.2.0769
- Lee, C., Yang, W., & Parr, R. G. (1988). Development of the Colle-Salvetti correlation-energy formula into a functional of the electron density. *Physical Review B*, *37*(2), 785.
- Li, B., Liu, Y., Luo, J., Cai, Y., Chen, M., & Wang, T. (2023). Contezolid, a novel oxazolidinone antibiotic, may improve drug-related thrombocytopenia in clinical antibacterial treatment. *Frontiers in Pharmacology, 14*, 1157437. https://doi.org/10.3389/fphar.2023.1157437
- Liu, B.-G., Yuan, X.-L., He, D.-D., Hu, G.-Z., Miao, M.-S., & Xu, E.-P. (2020). Research progress on the oxazolidinone drug linezolid resistance. *European Review for Medical and Pharmacological Sciences*, 24, 9274–9281.
- Lombardi, A., Pappas, F., Bruinenberg, P., Nedelman, J., Taneja, R., Hickman, D., Beumont, M., & Sun, E. (2025). *Pharmacokinetics, tolerability, and safety of*

- TBI-223, a novel oxazolidinone, in healthy participants. Antimicrobial Agents and Chemotherapy, 69(4), 1–17. https://doi.org/10.1128/aac.01542-24
- Madalambika, T. N. Lohith, N. S., Kameshwar, V. H., Kothanahally, S. S. Kumar, Ali, M. S., Al-Lohedan, H. A., Vinay Kumar, D. C., & Verma, S. K. (2025). Structural analysis and computational studies of pyrazole derivative: Investigation of interactions by X-ray crystallography, DFT, molecular docking, and molecular dynamics simulation. *Journal of Molecular Structure*, 1348(2), 143497. https://doi.org/10.1016/j.molstruc.2025.143497
- Mahdi, A. S., Alani, B. G., & Ibrahim, I. T. (2023). Oxazolidinones antibiotics, chemistry, applications and role in COVID-19 treatment. *Pharmacology & Pharmacy*, 14(1), 19–32. https://doi.org/10.4236/pp.2023.141002
- Mahmudov, I., Demir, Y., Sert, Y., Abdullayev, Y., Saleh, S. A., Alwasel, A., & Gulçin, İ. (2022). Synthesis and inhibition profiles of N-benzyl- and N-allyl aniline derivatives against carbonic anhydrase and acetylcholinesterase: A molecular docking study. *Arabian Journal of Chemistry*, 15(3), 103645. https://doi.org/10.1016/j.arabjc.2021.103645
- Malik, M. S., Faazil, S., Alsharif, M. A., Sajid Jamal, Q. M., Al-Fahemi, J. H., Banerjee, A., Chattopadhyay, A., Pal, S. K., Kamal, A., & Ahmed, S. A. (2023). Anti-bacterial properties and computational insights of potent novel linezolid-based oxazolidinones. *Pharmaceuticals*, *16*(4), 516. https://doi.org/10.3390/ph16040516
- Murray, J. S., & Politzer, P. (2011). The electrostatic potential: An overview. *Wiley Interdisciplinary Reviews: Computational Molecular Science*, 1, 153–163. https://doi.org/10.1002/wcms.24
- Nwobodo, C. D., Ugwu, M. C., Anie, C. O., Al-Ouqaili, M. T. S., Ikem, J. C., Victor, C. U., & Saki, M. (2022). Antibiotic resistance: The challenges and some emerging strategies for tackling a global menace. *Journal of Clinical Laboratory Analysis*, *36*(9), e24655. https://doi.org/10.1002/jcla.24655
- Pathania, S., Petrova Szczasiuk, K., Pentikäinen, O., & Singh, P. K. (2023). Oxazolidinones: Are they only good for the discovery of antibiotics? A worm's eye view. *Journal of Molecular Structure*, *1286*, Article 135630. https://doi.org/10.1016/j.molstruc.2023.135630
- Poturcu, K., & Çubuk Demiralay, E. (2019). Bazı heterosiklik bileşiklerin iyonlaşma/ protonasyon, lipofilisite ve çözünürlük sabitlerinin belirlenmesi. *Süleyman Demirel Üniversitesi Fen Bilimleri Enstitüsü Dergisi*, 23(2), 651–657. https://doi.org/10.19113/sdufenbed.553547
- Prasad, A. V. G. S., & Patel, F. (2024). A review on medicinally important nitrogen heterocyclic compounds. *International Journal of Novel Research and Development*, 9(6), 823–828.
- Qadir, T., Amin, A., Sharma, P. K., Jeelani, I., & Abe, H. (2022). A review on medicinally important heterocyclic compounds. *The Open Medicinal Chemistry Journal*, 16, e187410452202280. https://doi.org/10.2174/18741045-v16-e2202280

- Rani, P., Pal, D., Hegde, R. R., & Bhargava, S. (2021). New mercaptoacetamide derivatives: Synthesis and assessment as antimicrobial and antimycobacterial agents. *Pharmaceutical Chemistry Journal*, 55(7), 715–723. https://doi.org/10.1007/s11094-021-02483-0
- Roger, C., Roberts, J. A., & Muller, L. (2018). Clinical pharmacokinetics and pharmacodynamics of oxazolidinones. *Clinical Pharmacokinetics*, *57*(5), 559–575. https://doi.org/10.1007/s40262-017-0601-x
- Sabah, Y. H. (2014). Synthesis, characterization and biological evaluation of penicillin derivatives complexes with some metal ions (Master's thesis, Al-Mustansirya University).
- Shah, M., Suhagia, B., Goswami, S., Sagar, S., & Patwari, A. (2025). Novel tetracycline hybrids: Synthesis, characterization, docking studies and in vitro evaluation of antibacterial activity. *Future Journal of Pharmaceutical Sciences*, *11*, Article 10. https://doi.org/10.1186/s43094-025-00764-z
- Sharma, N., Banerjee, J., Shrestha, N., & Chaudhury, D. (2015). A review on oxazolone, its method of synthesis and biological activity. *European Journal of Biomedical and Pharmaceutical Sciences*, 2(3), 964–987.
- Shivaji, B. G., & Kasabe, A. J. (2021). Review of heterocyclic compound synthesis and antibacterial activity. *Journal of Pharmaceutical Negative Results*, 12(1), 98–102. ttps://doi.org/10.47750/pnr.2021.12.01.15
- Strydom, N., Ernest, J. P., Imperial, M., Solans, B. P., Wang, Q., Tasneen, R., Tyagi, S., Soni, H., Garcia, A., Bigelow, K., Gengenbacher, M., Zimmerman, M., Xie, M., Sarathy, J. P., Yang, T. J., Dartois, V., Nuermberger, E. L., & Savic, R. M. (2024). Dose optimization of TBI-223 for enhanced therapeutic benefit compared to linezolid in antituberculosis regimen. *Nature Communications*, *15*, Article 7311. https://doi.org/10.1038/s41467-024-43135-1
- Tariq, S., Rizvi, S. F. A., & Anwar, U. (2018). Tetracycline: Classification, structure activity relationship and mechanism of action as a theranostic agent for infectious lesions—A mini review. *Biomedical Journal of Scientific & Technical Research*, 7(4), 1–6. https://doi.org/10.26717/BJSTR.2018.07.001475
- Taylor, A. P., Robinson, R. P., Fobian, Y. M., Blakemore, D. C., Jones, L. H., & Fadeyi, O. (2016). Modern advances in heterocyclic chemistry in drug discovery. *Organic & Biomolecular Chemistry*, 14(28), 6611–6637. https://doi.org/10.1039/C6OB00936K
- Wang, C., Xiong, Y., Bao, C., Wei, Y., Wen, Z., Cao, X., Yu, Z., Deng, X., Li, G., & Deng, Q. (2023). Antibacterial and anti-biofilm activity of radezolid against *Staphylococcus aureus* clinical isolates from China. *Frontiers in Microbiology*, 14, 1131178. https://doi.org/10.3389/fmicb.2023.1131178
- Wang, T., Zhang, H., Feng, R., Ren, J., Xu, X., & Sun, S. (2025). The in vitro antimicrobial activity of linezolid against unconventional pathogens. *PeerJ*, *13*, e18825. https://doi.org/10.7717/peerj.18825
- Wang, W., Voss, K. M., Liu, J., & Gordeev, M. F. (2021). Nonclinical evaluation of

- antibacterial oxazolidinones Contezolid and Contezolid acefosamil with low serotonergic neurotoxicity. *Chemical Research in Toxicology*, *34*(5), 1348–1354. https://doi.org/10.1021/acs.chemrestox.0c00524
- Wei, L., Hong, M., Lu, M., Qian, Y., Li, Q., Tang, N., Li, H., Chang, Y., & Qiu, Y. (2025). Safety evaluation of Contezolid (MRX I) versus Linezolid in Sprague Dawley rats. *Drugs in R&D*, 25, 127–140. https://doi.org/10.1007/s40268-025-00504-x
- Wookey, A., Turner, P. J., Greenhalgh, J. M., Eastwood, M., Clarke, J., & Sefton, C. (2004). AZD2563, a novel oxazolidinone: Definition of antibacterial spectrum, assessment of bactericidal potential and the impact of miscellaneous factors on activity in vitro. *Clinical Microbiology and Infection*, 10(3), 247–254. https://doi.org/10.1111/j.1198-743x.2004.00770.x
- Xu, G., Zhou, Y., Yang, C., & Xie, Y. (2008). A convenient synthesis of oxazolidinone derivatives linezolid and eperezolid from (S)-glyceraldehyde acetonide. *Heteroatom Chemistry*, 19(3), 316–319. https://doi.org/10.1002/hc
- Zhang, G. X., Liu, T. T., Ren, A. X., Liang, W. X., Yin, H., & Cai, Y. (2024). Advances in Contezolid: Novel oxazolidinone antibacterial in Gram-positive treatment. *Infection*, 52(3), 787–800. https://doi.org/10.1007/s15010-024-02287-w



INVESTIGATION OF THE EFFECTS OF MAGNESIUM HYDROXIDE ON THE BORON NITRIDE FORMATION AT THE SOLID STATE METHODS





Muhammed ÖZ¹

¹ Assoc. Prof. Dr. Bolu Abant İzzet Baysal University, Gerede Vocational School, Chemistry and Chemical Processing Technology, oz_m@ibu.edu.tr, ORCID: 0000-0003-0049-0161.

1. Introduction

Boron nitride (BN) is a versatile ceramic material that has attracted growing interest in materials science and engineering due to its wide range of polymorphs and unique physical, chemical, and electronic properties. Structurally, BN exhibits polymorphism analogous to that of carbon, existing in hexagonal (h-BN), cubic (c-BN), rhombohedral (r-BN), and wurtzite (w-BN) phases (Vel, Demazeau, & Etourneau, 1991; Öz, 2020; Öz, 2021). Among these, hexagonal BN (h-BN) is the most stable at ambient conditions and is characterized by a layered, graphite-like structure in which strong in-plane B-N covalent bonds are coupled with weak van der Waals interactions between layers. This structure imparts h-BN with high anisotropy in thermal and electrical properties, excellent lubrication characteristics, and chemical inertness even in aggressive environments (Ouyang et al., 2022; Mog, Debnath, & Saha, 2025; Yadav, Kamboj, & Poonia, 2025). This polymorphic diversity, combined with a wide bandgap, high thermal conductivity, and resistance to chemical attack, makes BN a material of considerable technological interest (Caldwell et al., 2019; Mog, 2024).

The unique properties of BN have enabled its use in a wide spectrum of applications. h-BN, with its high thermal conductivity and electrical insulation, is widely employed in electronic packaging, heat spreaders, and substrates for two-dimensional (2D) electronics (Zhang et al., 2017; Caldwell et al., 2019). It is also used as a lubricant in high-temperature environments, owing to its structural analogy to graphite but with oxidation resistance up to ~1200 °C in air (Öz, 2020; Zhu, et al, 2022). Furthermore, BN is explored in the field of energy storage and conversion, including as a dielectric layer in capacitors, protective coatings for electrodes, and catalyst supports (Jang et al., 2016; Lu et al., 2022; Naclerio, & Kidambi, 2023).

Despite its promising applications, the large-scale production of high-quality BN remains challenging (Mirzaee, Rashidi, Zolriasatein, & Abadchi, 2021; Naclerio, & Kidambi, 2023). Conventional synthesis methods include carbothermal reduction–nitridation (CRN) of boron oxide (B₂O₃) with carbon in a nitrogen atmosphere, direct nitridation of elemental boron, and chemical vapor deposition (CVD) routes (Matsuda, Uno, Nakae, & Hirai, 1986; Rao & Kaner, 1994; Çamurlu, Topkaya, & Sevinç, 2009; Ahmad, Khandaker, Khan, & Amin, 2015; Ma, Bando, & Sato, 2001). While these methods are well established, they often require high processing temperatures (above 1500 °C), extended reaction times, and stringent atmospheric controls. These conditions not only increase energy consumption but also complicate scale-up for industrial production.

Moreover, carbothermal routes are prone to the formation of undesired secondary phases such as boron carbide (B₄C) and magnesium salts when

additives are employed, leading to a reduction in BN purity (Wood et al., 2005; Çamurlu, Topkaya, & Sevinç, 2009; Zhu, Li, Mei, & Qian, 2011). Particle agglomeration, poor control over crystallinity, and difficulties in tailoring morphology further limit the material's functional performance (Wang, Sun, Xu, & Qian, 2011). Thus, identifying strategies to reduce reaction barriers, enhance yield, and improve the structural quality of BN remains a critical research direction.

The incorporation of metallic or oxide additives has been investigated as a strategy to facilitate BN formation (Örnek et al., 2019). Magnesium-based compounds have shown considerable promise. Among these, magnesium hydroxide $Mg(OH)_2$ has drawn attention due to its decomposition behavior and multifunctional role during high-temperature processing (Iwasaki, Kodani, & Koga, 2020; Kumar, & Soren, 2023).

The in-situ generated MgO plays multiple roles in the BN formation process. First, it can act as a catalyst by enhancing the diffusion of nitrogen species and facilitating the nitridation of boron-containing precursors. Second, MgO may serve as a dispersing agent, limiting particle agglomeration and promoting the formation of finer, more uniform BN particles (Çamurlu, 2011; Iwasaki, Kodani, & Koga, 2020; Öz, 2021). Third, MgO can react with intermediate species during carbothermal processes, thereby reducing the formation of unwanted secondary phases and shifting the reaction pathway toward BN.

Meanwhile, the release of water vapor modifies the local atmosphere during heating, which can influence the kinetics of precursor decomposition and nitridation reactions. In some cases, Mg-containing intermediates such as magnesium borates may temporarily form and subsequently decompose, contributing further to BN crystallization (Kojima, Nose, Kambara, & Yoshida, 2009). Overall, the role of $\mathrm{Mg}(\mathrm{OH})_2$ is not merely as an additive but as a reactive agent that dynamically influences phase evolution, reaction kinetics, and microstructural development.

Although the beneficial effects of magnesium compounds on BN formation have been reported, there remain significant gaps in understanding the precise mechanisms by which ${\rm Mg(OH)}_2$ influences the process. Most prior studies have focused on MgO or Mg-based fluxes (Singhal, Echeverria, McIlroy, & Singh, 2022; Agarwal, Jensen, Chen, Rioux, & Matsoukas, 2022), while systematic investigations into the direct role of ${\rm Mg(OH)}_2$ remain limited. Key questions regarding its influence on reaction thermodynamics, intermediate phase formation, and final BN morphology are yet to be fully addressed. Additionally, the optimization of synthesis parameters, such as ${\rm Mg(OH)}_2$ content, and atmosphere, requires further exploration to maximize yield and purity.

The present study aims to illuminate the contribution of Mg(OH)₂ to the formation of BN. Special emphasis is placed on understanding how the thermal decomposition of Mg(OH)₂ and the subsequent presence of MgO affect phase evolution, and microstructural characteristics of BN. By clarifying the mechanistic role of Mg(OH)₂, this work seeks to provide new insights into designing energy-efficient and scalable synthesis strategies for high-quality BN materials. Ultimately, such an understanding will support the advancement of BN-based technologies in electronics, coatings, and high-temperature ceramics.

2. Materials and Methods

In the current study, BN has been synthesized by solid state method especially known as O'Connor method (O'Connor, 1962). The process is composed of the mixing of solid starting materials that are boron oxide, urea and magnesium hydroxide with a distinct range (1-40 % (w/w)) without any purification process. The preferred chemicals have purity of 99,9 % and above. The synthesis process has taken place in two steps. First one includes heating the occupied mixture at 200 °C and second one contains high temperature annealing at 1450 °C in the reactive ammonia gas. There is a homogenization process for 30 min. between heating periods. Finally, a purification section has been practiced by Acid leaching with 10 % HCl solution. After the samples have been prepared at the high temperature annealing process, characterization has been carried out by the FT-IR, XRD, SEM, and EDS (Öz, 2013, Öz, Sarıtekin, Bozkurt, & Yıldırım, 2016, Öz, 2025).

3. Results and Discussion

The structural, electronic, and optical properties of boron nitride (BN) are highly sensitive to foreign atom incorporation, making doping an effective strategy to tailor its physicochemical characteristics for advanced applications. Addition of metal hydroxides such as magnesium hydroxide ${\rm Mg(OH)}_2$ offers a promising pathway to overcome the limitations of interaction of boron oxide and urea by inducing local distortions, modifying charge distribution, and tuning the band gap.

In the present study, Mg(OH)₂ additive was introduced into the BN lattice to investigate its influence on structural stability, bonding characteristics, and electronic performance. The results provide insight into how Mg(OH)₂ incorporation alters lattice parameters, electron density distribution, and defect states, thereby affecting the material's optical absorption and electronic transport properties. A comparative analysis with pristine BN highlights the role of Mg(OH)₂ as a potential additive in enhancing active sites for catalytic activity. The following section discusses experimental outcomes in detail, focusing on analysis of Mg(OH)₂-doped BN via crystallite size, grain size, lattice parameters, etc. These findings contribute to a deeper understanding

of Mg(OH)₂ additive engineering in BN and provide a basis for its target use in next generation nano applications.

At first sight $Mg(OH)_2$ undergoes thermal decomposition at relatively low temperatures (~350-400 °C), producing magnesium oxide (MgO) and water vapor according to equation 1. It is found that the thermal decomposition of $Mg(OH)_2$ to MgO takes place as distorted cubic and cubic when it is conducted in the following sequence at 380 °C and 600 °C, respectively (Iwasaki, Kodani, & Koga, 2020).

$$Mg(OH)_{2(s)} \rightarrow MgO_{(s)} + H_2O_{(g)}$$
 Eq. 1

Boron oxide (B_2O_3) begins to melt approximately 450 °C and 510 °C depending on the crystalline nature as trigonal and tetrahedral, respectively. At this respect the boron oxide and $Mg(OH)_2$ possesses approximately close melting and decomposition properties respectively. That means the removal of water from $Mg(OH)_2$ possibly propagated the formation of starting monomer form of BN which obtained the reaction of the urea and B_2O_3 . In addition, $Mg(OH)_2$ in the converted form MgO might supply a surface for main source of boron and nitrogen or behave as a catalyst for decreasing the formation temperature of BN which was achieved at the 1600 °C and above in literature (O'Connor, 1962). It is clear that hBN synthesis is accomplished with $Mg(OH)_2$ at a lower temperature that is given in literature by the solid state method. The results of the applied instrumental methods will be given at the following section.

3.1.FT-IR Analysis

The Fourier-transform infrared (FT-IR) spectra of the synthesized samples provide clear evidence for the formation of BN and help pathway the role of $Mg(OH)_2$ during processing. In the precursor mixtures, characteristic absorption bands of B-O vibrations (typically around 1350-1450 cm⁻¹) and hydroxyl groups (broad band near 3400 cm⁻¹) were detected, indicating the presence of boron oxide and $Mg(OH)_2$. Upon heat treatment, these bands gradually diminished in intensity, confirming the decomposition of $Mg(OH)_2$ and the consumption of boron oxide during nitridation.

After nitridation by ammonia at elevated temperatures, the spectra discover two dominant absorption bands corresponding to h-BN: the in-plane B-N stretching vibration near \sim 1380-1440 cm⁻¹ and the out-of-plane B-N-B bending vibration at \sim 780-820 cm⁻¹ (Haubner, Wilhelm, Weissenbacher, & Lux, 2002; Öz, 2021). The sharpness and intensity of these peaks increased with amount of the Mg(OH)₂ additive, suggesting an improvement in crystallinity. Importantly, the absence or significant reduction of residual B-O bands in the final products indicate that Mg(OH)₂ effectively facilitated the conversion of boron precursors to BN. A weak absorption in the 3412

cm⁻¹ range is attributed to adsorbed moisture or surface hydroxyl groups or N-H vibration bands (Figure 1). Moreover, the inter platelet vibrations of the BN are observed in the range of 791-810 cm⁻¹ while intraplanar vibrational bands exist at around 1397-1424 cm⁻¹ depending on the amount of $Mg(OH)_2$ additive. In Fig. 1, the amount dependency clearly observed that intraplanar vibration frequency decreases as a result of tight binding of B-N however interplanar frequency increases as a consequence of the diminish at van der Waals interaction by the rise at the $Mg(OH)_2$ concentration. Overall, the FT-IR results confirm that $Mg(OH)_2$ contributes to the complete formation of hBN while suppressing oxygen-containing impurities.

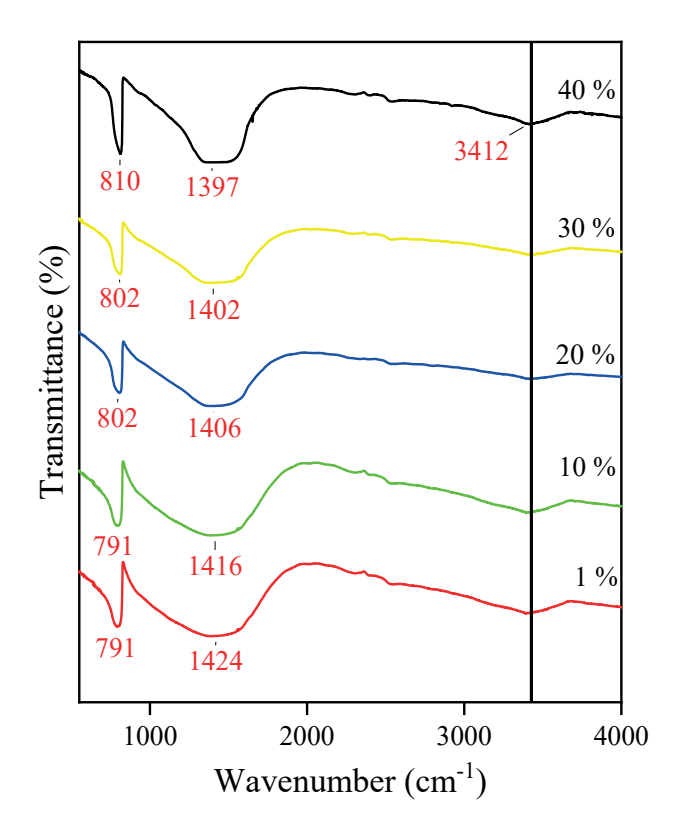


Figure 1. The FT-IR spectra of the hBN with Mg(OH)₂ additives with different amounts

3.2. XRD Analysis

The X-ray diffraction (XRD) patterns further validate the phase composition and structural evolution of the synthesized powders. At low amounts of additives, weak and broad diffraction peaks corresponding to hexagonal BN began to appear at $2\theta \approx 26.7^{\circ}$ (002), 41.6° (100), 43.8° (101), 50.2° (102), 76.0° (110), and 82.0° (112), although the crystallinity remained relatively

poor (Figure 2). With increasing amounts of the ${\rm Mg(OH)_2}$, the BN peaks become sharper and more intense, reflecting progressive crystallization of the h-BN phase At the 10 % addition level, the diffraction pattern is dominated by h-BN reflections, while another phase of BN coexists. The broad peaks of 100 and 101 is the observation of overlapping situations of hexagonal and turbostratic or nanostructure phases (Thomas, Weston, & O'connor, 1962).

Notably, the relative intensity of BN peaks is found to be significantly higher in samples prepared with Mg(OH)₂ compared to those synthesized without additives (3.61 nm), indicating that Mg(OH)₂ plays a catalytic role in enhancing BN formation. The calculated grain sizes from the (002) reflection using the Debye-Scherrer equation suggested that the BN particles were nanocrystalline in nature (Table 1), with grain sizes changes with additives (~9.1-11.2 nm). These findings confirm that Mg(OH)₂ promotes BN grain size (3.45 nm when it is synthesized by only boron oxide and urea) by reducing the activation energy barrier of the nitridation reaction. In addition, the number of plates is determined depending on the average grain size and the distance between the layers was determined to be around 30-33.

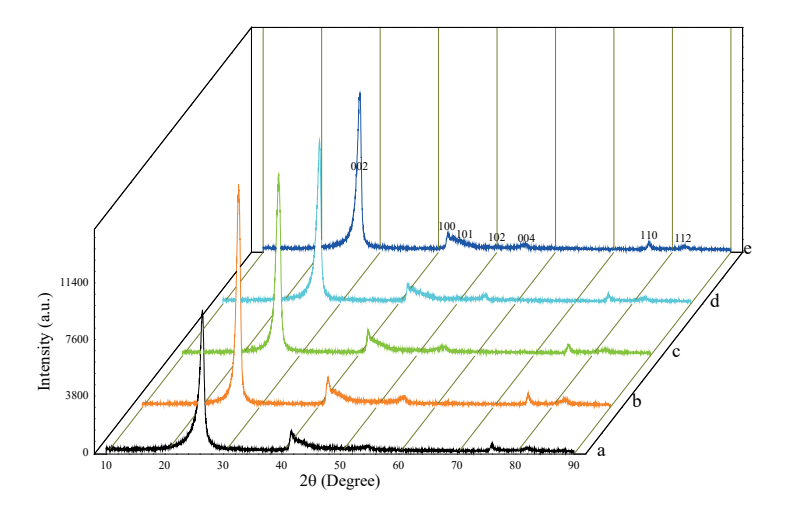


Figure 2. The XRD diffractograms of the hBN with $Mg(OH)_2$ additives in the value; a) 1, b) 10, c) 20, d) 30, e) 40%.

30 %

40 %

Dopant Level	Lattice	e Paramete	rs (nm)	Average Grain Size (nm)	Number of plates
	a=b	с	d		
1 %	0.2504	0.6736	0.3368	10.081	30
10 %	0.2502	0.6732	0.3366	11.161	33
20 %	02502	0.6742	0.2271	0.120	27

9.138

10.679

10.840

32

32

0.3371

0.3358

0.3360

Table 1. Crystallinity parameters of magnesium hydroxide added samples

3.3. SEM imagination

02502

0.2504

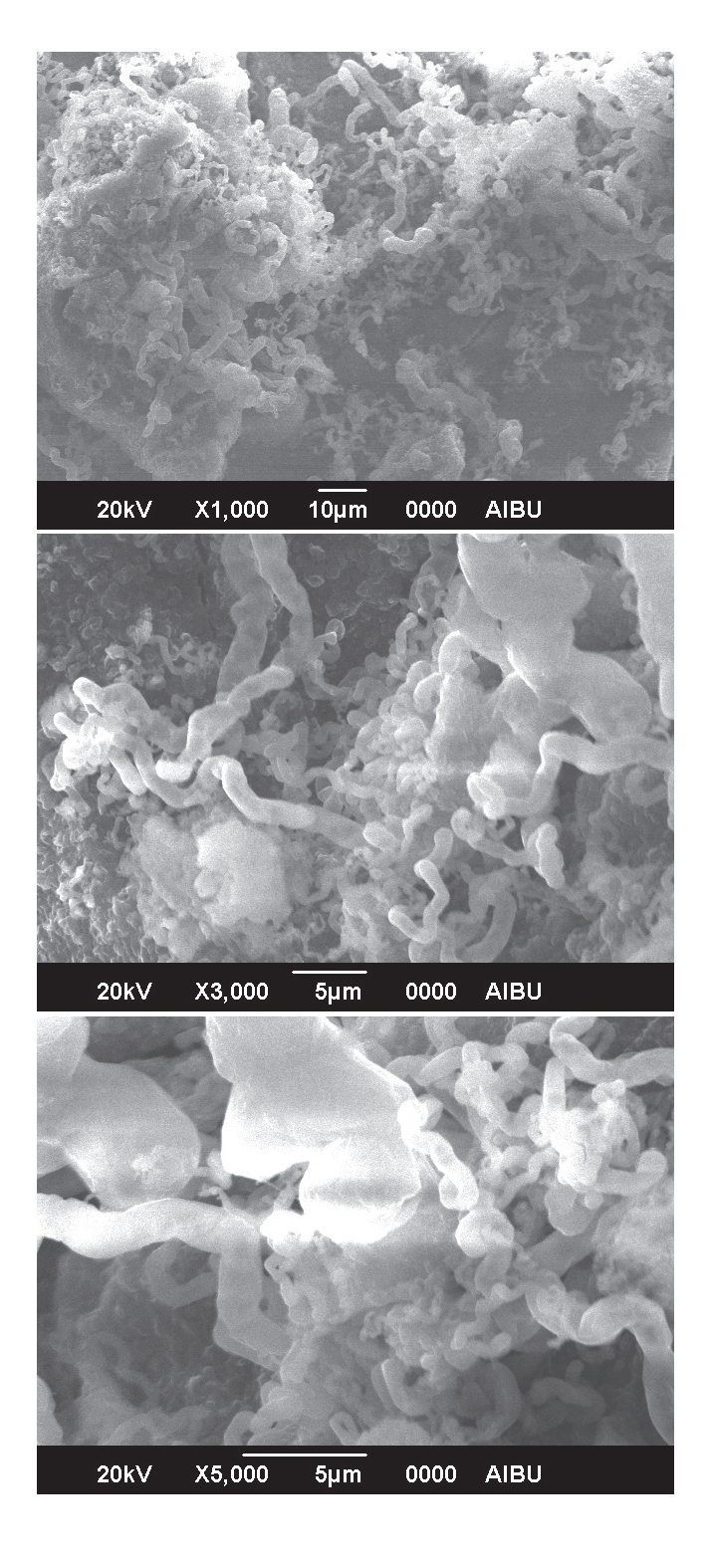
0.2506

0.6742

0.6716

0.6720

The surface morphology of the synthesized powders was examined by scanning electron microscopy (SEM). At higher imaginations (10000 fold), the BN particles appeared as thin platelets with relatively smooth surfaces, aligned and stacked into larger aggregates (Figure 3). This morphology is typical for hexagonal BN and supports the FT-IR and XRD results. The presence of MgO particles is very limited, possibly dispersed grains embedded between BN platelets, suggesting that Mg(OH)₂ acted as a dispersant that prevented excessive particle growth and agglomeration. This effect contributed to the formation of finer BN powders with improved uniformity compared to BN synthesized without Mg(OH)₂. At relatively lower imaginations, SEM images of the magnesium hydroxide doped hBN samples is in the form of helix structure on the planar surface which means of the tubular three-dimensional framework. The contribution of magnesium hydroxide has significantly been exhibited by SEM visualizations. The results indicate that hBN has been successfully synthesized by this method with high crystalline nanostructure.



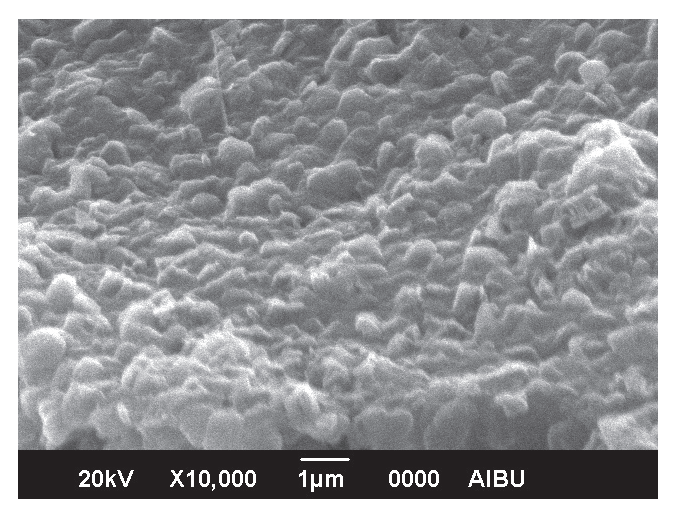


Figure 3. The SEM visualization of Mg(OH), added hBN

3.4. EDS interpretation

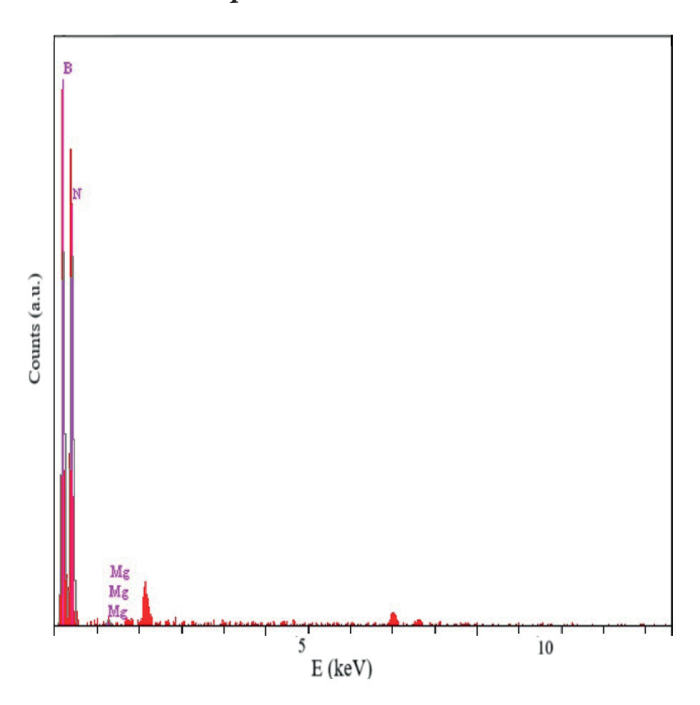


Figure 5. One of the EDS spectra of the hBN with Mg(OH), additives

The Energy Dispersive X-ray Spectroscopy (EDS) analysis is performed to confirm the elemental composition and purity of the synthesized hBN sample. The EDS spectrum stated the presence of two prominent peaks corresponding to boron (B) and nitrogen (N) elements (as given in figure 5) with 57 and 42.83

% respectively, which are characteristic constituents of boron nitride. The very low ratio of the magnesium found as 0.03 % can be assumed as negligible and any significant peaks related to oxygen, carbon, or other impurities indicate the high purity of the synthesized material (Table 2). Overall, the EDS results validate the successful formation of BN and confirm that the sample is free from detectable levels of foreign elements or contamination. This compositional purity is essential for ensuring the desirable electronic, thermal, and mechanical properties of BN-based materials.

Element	Intensity (c/s)	Concentration (wt %)
В	111.67	57.147
N	111.54	42.826
Mg	2.13	0.026

Table 2. The elemental composition of BN determined by EDS

The combined results of FT-IR, XRD, SEM, and EDS analyses demonstrate that $\mathrm{Mg(OH)}_2$ plays a significant role in promoting BN formation. Its decomposition to MgO and water vapor not only facilitates precursor reactivity but also improves BN crystallinity and morphology. The in-situ MgO acts as both a catalyst and a structural dispersant, enhancing nitrogen diffusion and reducing agglomeration of BN platelets. Consequently, the presence of $\mathrm{Mg(OH)}_2$ accelerates phase evolution, suppresses oxygencontaining impurities, and leads to nanostructured BN with improved structural integrity.

4. Conclusion

This study demonstrates that Mg(OH), plays a decisive role in facilitating the synthesis and structural development of boron nitride. The FT-IR spectra confirmed the progressive disappearance of boron-oxygen and hydroxyl vibrations and the emergence of characteristic B-N bands, indicating that Mg(OH), enhances the complete transformation of boron precursors into BN. XRD analysis revealed the decomposition of Mg(OH), into MgO, followed by the gradual crystallization of hexagonal BN. The presence of sharper and more intense BN reflections in Mg(OH), assisted samples highlights its catalytic effect in promoting phase evolution and improving grain size. SEM observations further supported these findings, showing that Mg(OH), suppresses agglomeration, promotes the growth of thin BN platelets, and yields powders with a more uniform and controlled microstructure. Besides, these results suggest that the decomposition products of Mg(OH),, particularly MgO, play different roles: enhancing diffusion kinetics, stabilizing intermediate phases, and dispersing BN platelets during growth. As a result, the use of Mg(OH), not only lowers the

energy barrier for BN formation but also improves the structural quality and morphology of the final product.

Further research is needed to optimize synthesis parameters and fully exploit its potential while the current study confirms the beneficial role of Mg(OH)₂ in promoting BN formation. Future studies should focus on systematically investigating the influence of Mg(OH)₂ content, heating rate, and nitridation atmosphere on phase evolution and crystallinity. Quantitative studies on the kinetics of BN formation in the presence of Mg(OH)₂ would also help clarify the mechanistic pathways involved. Additionally, advanced characterization techniques such as transmission electron microscopy (TEM), and thermogravimetric analysis (TGA) could provide deeper insight into intermediate phases and surface chemistry during the reaction process.

REFERENCES

- Agarwal, P. P., Jensen, D., Chen, C. H., Rioux, R. M., & Matsoukas, T. (2022). Synthesis and characterization of magnesium/boron solid solutions for energetic applications. *ACS Applied Energy Materials*, 5(6), 6716-6723.
- Ahmad, P., Khandaker, M. U., Khan, Z. R., & Amin, Y. M. (2015). Synthesis of boron nitride nanotubes via chemical vapour deposition: A comprehensive review. *RSC advances*, 5(44), 35116-35137.
- Caldwell, J. D., Aharonovich, I., Cassabois, G., Edgar, J. H., Gil, B., & Basov, D. N. (2019). Photonics with hexagonal boron nitride. *Nature Reviews Materials*, 4(8), 552-567.
- Çamurlu, H. E. (2011). Effect of Na₂CO₃ on hexagonal boron nitride prepared from urea and boric acid. *Ceramics International*, *37*(6), 1993-1999.
- Çamurlu, H. E., Topkaya, Y., & Sevinç, N. (2009). Catalytic effect of alkaline earth oxides on carbothermic formation of hexagonal boron nitride. *Ceramics International*, 35(6), 2271-2275.
- Haubner, R., Wilhelm, M., Weissenbacher, R., & Lux, B. (2002). Boron nitrides-properties, synthesis and applications. In *High performance non-oxide ceramics II* (pp. 1-45). Berlin, Heidelberg: Springer Berlin Heidelberg.
- Iwasaki, S., Kodani, S., & Koga, N. (2020). Physico-geometrical kinetic modeling of the thermal decomposition of magnesium hydroxide. *The Journal of Physical Chemistry C*, 124(4), 2458-2471.
- Jang, S. K., Youn, J., Song, Y. J., & Lee, S. (2016). Synthesis and characterization of hexagonal boron nitride as a gate dielectric. *Scientific reports*, *6*(1), 30449.
- Kojima, K., Nose, K., Kambara, M., & Yoshida, T. (2009). Effects of magnesium doping on growth and electric conductivity of nanocrystalline cubic boron nitride thin films. *Journal of Physics D: Applied Physics*, 42(5), 055304.
- Kumar, N., & Soren, S. (2023). Magnesium metal nano composites-A solid state hydrogen storage material. *Materials Today: Proceedings*.
- Lu, S., Shen, P., Zhang, H., Liu, G., Guo, B., Cai, Y., Chen, H., Xu, F., Zheng, T., Xu, F., Chen, X., Cai. D., & Kang, J. (2022). Towards n-type conductivity in hexagonal boron nitride. *Nature communications*, *13*(1), 3109.
- Ma, R., Bando, Y., & Sato, T. (2001). CVD synthesis of boron nitride nanotubes without metal catalysts. *Chemical Physics Letters*, 337(1-3), 61-64.
- Matsuda, T., Uno, N., Nakae, H., & Hirai, T. (1986). Synthesis and structure of chemically vapour-deposited boron nitride. *Journal of materials science*, 21(2), 649-658.
- Mirzaee, M., Rashidi, A., Zolriasatein, A., & Abadchi, M. R. (2021). A simple, low cost, and template-free method for synthesis of boron nitride using different precursors. *Ceramics International*, 47(5), 5977-5984.

- Mog, T. (2024). Advances of synthesis of hexagonal boron nitride for industrial applications: A review. *Materials International*, *6*(3), 23.
- Mog, T., Debnath, R., & Saha, M. (2025). Hexagonal boron nitride at low temperatures: controlled synthesis and mechanism. *Analytical Chemistry Letters*, *15*(1), 119-128.
- Naclerio, A. E., & Kidambi, P. R. (2023). A review of scalable hexagonal boron nitride (h-BN) synthesis for present and future applications. *Advanced Materials*, 35(6), 2207374.
- O'Connor, T. E. (1962). Synthesis of boron nitride. *Journal of the American Chemical Society*, 84(9), 1753-1754.
- Örnek, M., Wang, K., Xiang, S., Hwang, C., Xie, K. Y., & Haber, R. A. (2019). Molten salt synthesis of highly ordered and nanostructured hexagonal boron nitride. *Diamond and Related Materials*, 93, 179-186.
- Ouyang, J. H., Li, Y. F., Zhang, Y. Z., Wang, Y. M., & Wang, Y. J. (2022). High-temperature solid lubricants and self-lubricating composites: A critical review. *Lubricants*, 10(8), 177.
- Öz, M. (2013). Synthesis of hexagonal boron nitride in the existance of fluxing agents, Bolu, Bolu Abant İzzet Baysal Üniversitesi Fen Bilimleri Enstitüsü.
- Öz, M., Saritekın, N. K., Bozkurt, Ç., & Yildirim, G. (2016). Synthesis of highly ordered hBN in presence of group I/IIA carbonates by solid state reaction. *Crystal Research and Technology*, 51(6), 380-392.
- Öz, M. (2020). Temperature dependency on crystallinity and durability of mineral dolomite doped nanocrystalline hexagonal boron nitride. *Journal of Inorganic and Organometallic Polymers and Materials*, 30(3), 758-766.
- Öz, M. (2021). Characterization of caesium carbonate-doped porous non-activated graphitic (hexagonal) boron nitride and adsorption properties. *Arabian Journal for Science and Engineering*, 46(6), 5671-5680.
- Oz, M., (2025). Magnesium hydroxide contribution to the formation of ultra fine hexagonal boron nitrate by O'Connor model, 2nd International Conference on Sensor, Detector, Material Sciences and Technologies, October 09-11, 2025, Bolu, Türkiye
- Rao, L., & Kaner, R. B. (1994). Rapid solid-state-precursor synthesis of crystalline boron nitride. *Inorganic Chemistry*, *33*(15), 3210-3211.
- Singhal, R., Echeverria, E., McIlroy, D. N., & Singh, R. N. (2022). Chemical vapor deposition growth of magnesium-doped hexagonal boron nitride films via in situ doping. *Journal of Materials Research*, *37*(15), 2369-2377.
- Thomas, J. R., Weston, N. E., & O'connor, T. E. (1962). Turbostratic boron nitride, thermal transformation to ordered-layer-lattice boron nitride. *Journal of the American Chemical Society*, 84(24), 4619-4622.

- Vel, L., Demazeau, G., & Etourneau, J. (1991). Cubic boron nitride: synthesis, physicochemical properties and applications. *Materials Science and Engineering: B*, 10(2), 149-164.
- Wang, L., Sun, C., Xu, L., & Qian, Y. (2011). Convenient synthesis and applications of gram scale boron nitride nanosheets. *Catalysis Science & Technology*, 1(7), 1119-1123.
- Wood, G. L., Janik, J. F., Visi, M. Z., Schubert, D. M., & Paine, R. T. (2005). New borate precursors for boron nitride powder synthesis. *Chemistry of materials*, *17*(7), 1855-1859.
- Yadav, A., Kamboj, A., & Poonia, K. (2025). Fabrication and Applications of Hexagonal Boron Nitride (h-BN). In *2D Materials: Fundamentals, Fabrication, and Applications* (pp. 79-99). Singapore: Springer Nature Singapore.
- Zhang, K., Feng, Y., Wang, F., Yang, Z., & Wang, J. (2017). Two dimensional hexagonal boron nitride (2D-hBN): synthesis, properties and applications. *Journal of Materials Chemistry C*, 5(46), 11992-12022.
- Zhu, M., Li, G., Gong, W., Yan, L., & Zhang, X. (2022). Calcium-doped boron nitride aerogel enables infrared stealth at high temperature up to 1300° C. *Nano-Micro Letters*, *14*(1), 18.
- Zhu, Y., Li, Q., Mei, T., & Qian, Y. (2011). Solid state synthesis of nitride, carbide and boride nanocrystals in an autoclave. *Journal of Materials Chemistry*, 21(36), 13756-13764.